Archives of Computational Methods in Engineering (2024) 31:1363–1404
https://doi.org/10.1007/s11831-023-10020-3

ORIGINAL PAPER

Finite-Element Modelling of Needle-Tissue Interactions

Hossein Mohammadi[1,2] · **Arash Ebrahimian**[1,2] · **Nima Maftoon**[1,2]

Received: 14 November 2022 / Accepted: 7 October 2023 / Published online: 7 November 2023

Abstract
Needle insertion into soft biological tissues has been of interest to researchers in the recent decade due to its minimal invasiveness in diagnostic and therapeutic medical procedures. This paper presents a review of the finite-element (FE) modelling of the interaction of needle/microneedles with soft biological tissues or tissue phantoms. The reviewed models laid a solid foundation for developing more efficient novel medical technologies. This paper encompasses FE models for both invasive and non-invasive needle-tissue interactions. The former focuses on tissue and needle deformation without employing any damage mechanism, whereas the latter incorporates algorithms that enable crack propagation with a damage mechanism. Invasive FE models are presented in five categories, namely nodal separation, element failure/deletion, cohesive zone (CZ), arbitrary Lagrangian–Eulerian (ALE), and coupled Eulerian–Lagrangian (CEL) methods. In each section, the most important aspects of modelling, challenges, and novel techniques are presented. Furthermore, the application of FE modelling in real-time haptic devices and a survey on some of the most important studies in this area are presented. At the end of the paper, the importance and strength of the reviewed studies are discussed and the remaining limitations for future studies are highlighted.

1 Introduction

1.1 Background

Needles and microneedles have increasingly attracted attention in medical diagnosis and clinical therapies in recent decades. Their use in various medical procedures such as vaccinations, regional anesthesia injections, drug delivery, brachytherapy for cancer treatment, blood sampling, biopsy, neurosurgery, muscle and skin signal recording, virtual reality surgical systems, and surgical robots provided a considerable improvement in different stages of diagnosis and treatment [1–4] (Fig. 1).

The precision of percutaneous insertion plays an important role in the patients' safety and the diagnosis fidelity or treatment efficacy. The accuracy of tissue cutting with medical tools depends on the mechanical characteristics of the tissue, tool material and design, and operation mechanism. This is where numerical modelling comes into play. Modelling needle-tissue interactions not only can help developing novel medical devices but also can reduce the need for performing animal and human studies and their consequent economic and ethical issues. Finite-element (FE) method has been shown to be a remarkably powerful method for modelling of damage and injury in human and animal tissues [5–7].

In the investigation of needle-tissue interactions, various biological and non-biological soft tissues have been of interest to researchers. The skin, muscle, fat, liver, and brain are among the most popular biological tissues that have been investigated using FE modelling [8–11]. Most of these models exploited either the human skin due to easy accessibility or porcine organs due to their similarity to human tissues in terms of their micro structures and mechanical properties [12, 13]. Moreover, many studies used non-biological soft phantoms to mimic soft tissues for FE model developments [14, 15].

✉ Nima Maftoon
nmaftoon@uwaterloo.ca

Hossein Mohammadi
h.mohammadi@uwaterloo.ca

Arash Ebrahimian
arash.ebrahimian@uwaterloo.ca

[1] Department of Systems Design Engineering, University of Waterloo, Waterloo, ON, Canada

[2] Centre for Bioengineering and Biotechnology, University of Waterloo, Waterloo, ON, Canada

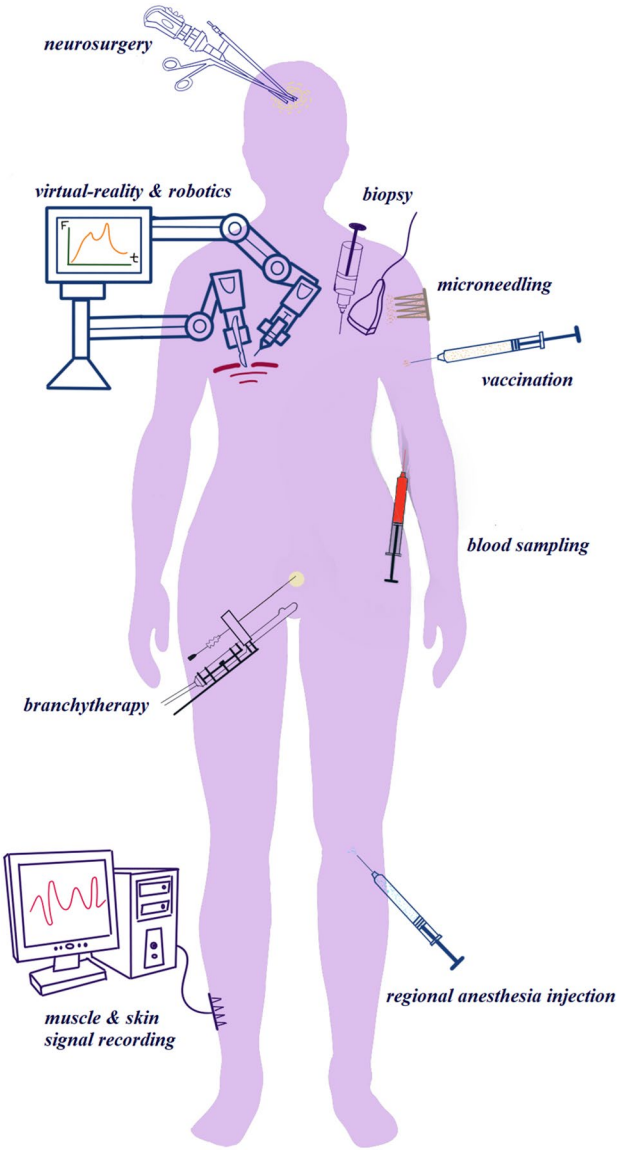

Fig. 1 The applications of needles and microneedles in medical diagnosis and treatment

1.2 Related Reviews

To date, there have been substantial advances in cutting soft tissues and needle intervention in medical applications. Some published reviews tried to survey these advances from different perspectives. Abolhassani et al. [16] conducted a survey on needle penetration into soft tissues that included studies on modelling of insertion forces, needle deflection, tissue deformation, and automated insertion procedures. With the development of robot-assisted procedures, numerous studies paid attention to the application of needles used in those procedures. For instance, Misra et al. [17] reviewed the literature of tool-tissue interaction models. They covered continuum mechanics for tissue modelling, FE modelling, non-invasive and invasive soft tissue deformation modelling as well as model acquisition methods and commercial surgical simulators.

Experimental studies of the interaction forces between a needle and tissue were reviewed by van Gerwen et al. [18]. They remarkably summarized data on needle axial force characteristics (magnitude, insertion phases, and force components) as well as the effects of insertion methods (manual vs. automated, velocity, axial rotation, location, and direction), needle characteristics (diameter, tip type, sharpness, and lubrication), and tissue characteristics (artificial vs. biological, human vs. non-human, live vs. dead) on the insertion procedure. In another survey, Wang et al. [19] summarized needle-tissue interaction studies surveying needle geometries, modelling approaches (e.g., mathematical models, FE simulations, and fracture mechanics approaches), design, manufacturing, and applications.

Recently, microneedles attracted the attention of researchers due to their advantages over hypodermic needles such as minimal invasiveness, less pain and irritation, simpler operation, and stability of therapeutic procedures [20, 21]. Ma and Wu [22] reviewed the studies that investigated biomicroneedles and bio-inspired microneedles. They classified various microneedles and discussed the insertion characteristics of microneedles into soft tissues and their efficiency for drug delivery.

Takabi and Tai [23] reviewed studies that described the cutting mechanics of tissues with various mechanical properties (i.e., soft tissues and bone) and related modelling techniques. Their review included both mathematical models (elemental cutting tool and fracture mechanics models) and computational models (FE analysis with cohesive zone and nodal separation models). Also, Liu et al. [24] reviewed the development of surgical blades for cutting soft biological tissues with a concentration on the different cutting mechanisms, optimization of the cutting parameters, the advances in surgical blades' material and structure, and the damage of tissue and blades. Some studies in the literature also focused specifically on bone cutting and needle insertion to bone tissue instead of soft tissues [25–27].

Robot-assisted surgical tools and haptic devices are among the applications that highly involve medical needles. Gao et al. [28] conducted a survey on different algorithms of needle steering techniques (e.g., nonholonomic systems, artificial potential field algorithm, virtual spring model, cantilever beam model). Such techniques can be used to facilitate target hitting, path planning, and desirable trajectory achievement. Ravali and Manivannan [29] also reviewed different models of needle insertion, tissue deformation, and their interactions for haptic technologies. The classical and dynamic friction models as well as the importance of psychophysics and corresponding psychophysical parameters

in designing needle simulators were covered in their study. Furthermore, a systematic review of the scientific and patent literature for needle-steering instruments was conducted by Scali et al. [30] in which distinguished mechanisms for the instrument deflection in either uncalled-for or on-demand situations were classified and the related design solutions were discussed. Li et al. [31] also reviewed the interactions between needle and tissue in image-guided robot-assisted surgical systems taking force modelling, surgical simulations, and steering control into account. Moreover, Corrêa et al. [32] reviewed studies on haptic interactions for virtual needle-insertion training simulations and covered different methodologies, types of environments, medical applications, devices, and haptic feedback.

1.3 Scope of This Review

In this review, we specifically focused on modelling tissue deformation and the cutting process using FE analysis, which is not only a powerful tool for modelling biomechanical procedures but also practical in many different cases where real experimental studies are not feasible. It also does not have medical and ethical challenges that experimental research on human and animals should usually deal with. Models of needle-tissue interactions can be classified into two general categories; namely, non-invasive and invasive models. In the first category, the deformation of tissue or needles prior to the tissue puncture or needle damage is considered while in the second category, a mechanism of failure is implemented in the model to enable the insertion of a needle (or any type of cutter) into the tissue.

This paper covers non-invasive and invasive approaches separately. In each section, the reviewed papers are mainly discussed in chronological order. Moreover, a brief survey of the most recent applications of FE models in real-time haptics is provided at the end of the paper.

1.4 Source of Reviewed Articles

The reviewed articles were primarily sourced from academic research databases including ScienceDirect, Google Scholar, PubMed, Web of Science, and Scopus. We conducted a comprehensive search using keywords (e.g., needle, biological tissue, soft tissue, finite element modelling, puncture, cutting, cohesive zone method, CZM, real-time haptics) and Boolean operators to ensure coverage of relevant literature.

1.5 Selection Criteria

The most important selection criterion for this review was relevance to the topic. Numerous studies have been conducted in the field of needle-tissue interactions that used various methods such as experimental, analytical, and numerical. However, the focus of the current review was only on numerical articles. Moreover, among all numerical methods studied in the literature like Finite Element Method (FEM), Finite Difference Method (FDM), Finite Volume Method (FVM), Boundary Element Method (BEM), and Monte Carlo Methods, we only focused on FEM studies. The other criterion was publication date within the last 15 years to ensure currency (more than 80% of the reviewed articles were published in the recent decade). We conducted all searches from September 2019 to October 2022.

2 Non-invasive Finite-Element Models

The earliest models in the literature of needle-tissue interactions are models in which no crack propagation happens in the tissue and consequently, the needle does not penetrate inside the tissue. Although some of these studies claim modelling the penetration procedure, they do not include a damage mechanism to account for the cutting procedure. Hereafter, we call these models non-invasive. The needle in these models either does not exist, is in external contact with the tissue, or is embedded in the tissue yet without the capability of inducing further crack propagation. The popularity of these models has had two main reasons: firstly, some applications do not require cutting tissues, and analyzing their deformation under the external load of the needle without crack propagation in the tissue gives enough information on needle-tissue interaction (e.g., finding needle reaction force preceding the tissue puncture and predicting tissue deformation under needle indentation). Secondly, fracture modelling in a soft tissue, as a complicated non-linear phenomenon, usually involves an immense computational cost and requires experimental measurements for validation.

Aoyagi et al. [33] used an FE model of microneedle insertion into the skin tissue to investigate stress concentration around the tip of microneedles of different shapes (i.e., straight, simple jagged, and harpoon shapes) and various widths and tip angles. To this end, they used both two-dimensional and three-dimensional FE models for the simulation of sharp microneedles and jagged shape microneedles imitating mosquito's proboscis. In their models, no failure criterion was incorporated into the tissue; instead, the microneedle was embedded in the tissue since the beginning. Their simulations were performed under a load-controlled condition by applying a constant force along the centerline of the needle and finding the stress distribution in the tissue. The needle was considered to be made of polylactic acid (PLA) and the skin tissue was modelled as silicone rubber with linear elastic material properties. Figure 2 exhibits stress distribution in the skin tissue caused by microneedle insertion in different geometrical and loading conditions. Due to symmetry, in their three-dimensional model, only a

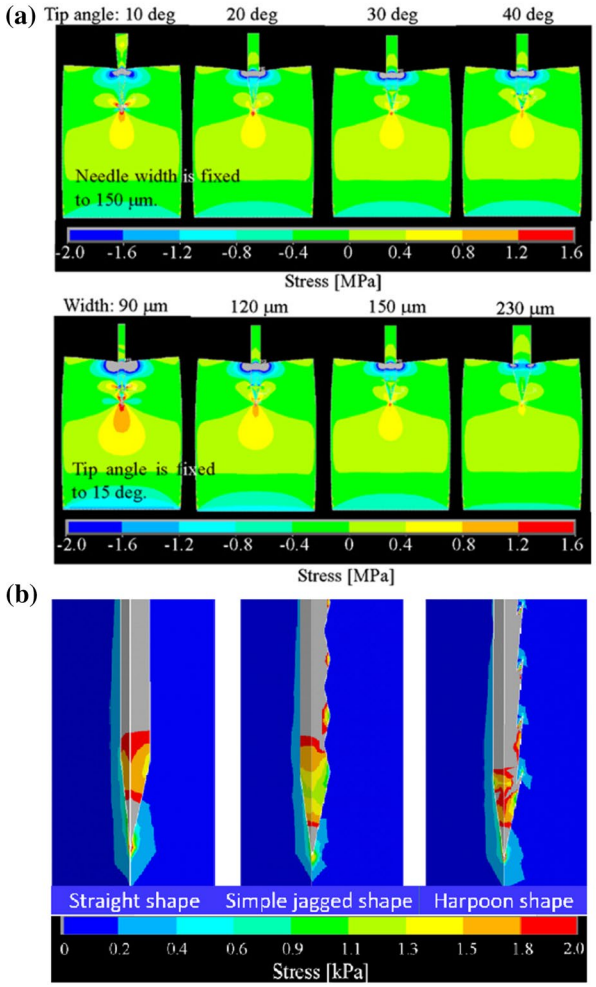

Fig. 2 Stress distribution in the artificial skin tissue (made of silicone rubber) around the microneedle insertion location obtained from FE modelling of the embedded needle in the silicone rubber without incorporation of any damage mechanism, Reprinted from [33] with permission from Elsevier: **a** the effect of tip angle (top) and width (bottom) on stress, **b** the effect of jagged shape on stress

quarter of the needle was considered in all simulations. The results showed sharper and thinner microneedles cause more severe stress concentration in the tissue leading to an easier penetration procedure. For more complicated jagged shape microneedles, however, the distribution of stress concentration is not always identical. Needles with a simple jagged shape cause stress concentration only around the needle tip in the tissue while for harpoon shape needles the stress concentration appears at the tip areas of the jagged protrusions. Multiple stress concentrations happening in the tissue by harpoon-shaped needles can be regarded as a more effective option for easy needle penetration.

Although in some tissues under specific loading conditions linear mechanical properties can imitate the stress–strain characteristics, the behaviour of most biological tissues can be captured more accurately using non-linear constitutive material models. Wittek et al. [34] employed a fully non-linear FE model that considered both geometrical and material nonlinearities using subject-specific constitutive properties to simulate needle insertion into the brain tissue. They implemented their proposed model on the swine brain and determined the constitutive properties experimentally. An Ogden hyper-viscoelastic material model proposed by Miller and Chinzei [35] was adopted to define the constitutive behaviour of the brain tissue. Based on their model, the strain-energy potential function (W) and shear modulus (μ) can be written as follows [36]:

$$W = \frac{2}{\alpha^2}\int_0^t \left[\mu(t-\tau)\frac{d}{d\tau}(\lambda_1^\alpha + \lambda_2^\alpha + \lambda_3^\alpha - 3)d\tau\right] \tag{1}$$

$$\mu = \mu_0\left[1 - \sum_{k=1}^{n} g_k(1 - e^{t/\tau_k})\right] \tag{2}$$

where λ_i represents the principal stretch and α is a real-valued material coefficient. Also, μ_0 is the instantaneous shear modulus and g_k and τ_k are the relaxation coefficient and characteristic time, respectively. Wittek et al. considered only two terms in Eq. 2 (i.e., n = 2).

Wittek et al. used magnetic resonance images to reconstruct the brain mesh from the swine brain. Eight-node hexahedral elements with hourglass control were exploited in their model. The pia matter (a tissue layer enveloping the brain) was modelled with Belytschko–Tsay shell elements [37] rigidly attached to the hexahedral elements and using the Mooney–Rivlin constitutive equation [38]:

$$W = \frac{C_1}{2}(I_1 - 3) + \frac{C_2}{2}(I_2 - 3) \tag{3}$$

where W is the strain-energy potential function, C_1 and C_2 are material constants and I_1 and I_2 are the invariants of the right Cauchy-Green deformation tensor. They assumed $C_1 = C_2$ and as shear modulus is $\mu = 2(C_1 + C_2)$, they needed only one parameter as $C_1 = C_2 = \frac{\mu}{4}$.

Instead of directly including the needle, they applied external boundary conditions on several pia matter nodes representing the needle tip. By this means, they analyzed the effect of needle indentation on the brain surface in the pre-puncture phase without incorporating any damage mechanisms.

Modelling the high-speed deformation of biological tissues, especially using complicated three-dimensional models with non-linear material properties, involves high computational costs. Therefore, it is necessary to choose a suitable numerical solver and an appropriate mesh type to obtain reliable results with high enough accuracy while minimizing the computational cost. Idkaidek and Jasiuk [39] simulated

the interaction of a surgical knife and the porcine liver using different implicit and explicit analysis schemes, as well as various element types and mesh densities in ABAQUS and investigated their effects on the computation time. A third-order polynomial form of Ogden hyperelastic material [40, 41] was assigned to the liver tissue:

$$W = \sum_{i=1}^{N} \frac{2\mu_i}{\alpha_i^2}\left(\overline{\lambda}_1^{\alpha_i} + \overline{\lambda}_2^{\alpha_i} + \overline{\lambda}_3^{\alpha_i} - 3\right) + \sum_{i=1}^{N} \frac{1}{D_i}(J^{del} - 1)^{2i} \quad (4)$$

where $\overline{\lambda}_i$ is the deviatoric principal stretch, J^{del} is the elastic volume ratio, and μ_i, α_i, D_i are material constants. The liver was defined as a nearly incompressible material using the material properties reported by Kemper et al. [42]. The surgical knife was modelled with elastic properties and compared with a rigid model of the knife, and from this comparison, the authors concluded that there are no noticeable differences between them in terms of simulation speed. The surgical knife was meshed with hexahedral elements, whereas different meshing strategies using either hexahedral or tetrahedral elements with various element sizes were considered for the tissue. The advantage of the explicit solver, convergence, usually comes with a high computational time. Idkaidek and Jasiuk [39] showed increasing the load rate (increasing the material strain rate artificially with the same load rate factor) or applying mass scaling (increasing the stable time increment by a factor of f while the material density increased artificially by a factor of f^2) to the FE model can significantly reduce the simulation time of the explicit solver but the results are only accurate if the inertia forces are insignificant.

The tissue displacement during the insertion process usually leads to a target motion and consequently, an abortive medical procedure. The target motion happens due to the interaction between the needle and tissue and can be captured using FE simulation. Oldfield et al. [43] explored the effects of different actuation mechanisms of the needle including direct push, reciprocal motion, and reciprocal motion with pullback in reducing target motion. They performed three-dimensional FE modelling of multi-segment needle insertion into a soft tissue with a pre-existing crack and verified their calculations using experiments of the insertion of a needle into a gelatin tissue phantom during which the target motion was measured using digital image correlation. The tissue phantom was modelled as a linearly elastic block and the needle was modelled as a four-part rigid body that inserts into the tissue with a pre-existing crack on a straight insertion trajectory along the needle axis. In their simulations, they also added a frictionless rigid collar inserted on the top surface of the tissue block to prevent excessive distortion or collapse of elements. Figure 3 shows the modelled tissue phantom with a pre-existing crack as well as the needle geometry and mesh. Coulomb friction

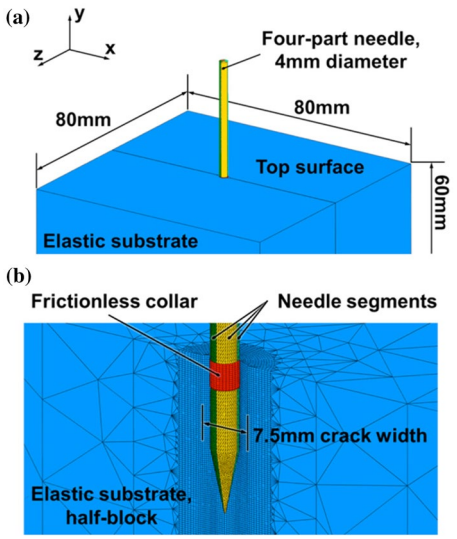

Fig. 3 FE modelling of needle-tissue interactions without incorporation of any damage mechanism in the gelatine tissue phantom [43]: **a** constructed elastic block of tissue a with a planar crack, **b** a cutting view of needle-tissue model representing the model mesh and crack dimensions

between needle segments and crack surfaces was established using a penalty contact algorithm. Two different types of elements including eight-node hexahedral reduced-integration elements and four-node tetrahedral elements were adopted for regions adjacent to the crack and parts away from the insertion region, respectively. All simulations were conducted using ABAQUS/Explicit solver under a quasi-static loading condition. They also used scaling in the insertion velocities to save computational time.

The strain in the tissue in interactions with a needle is associated with the patient's pain received by nociceptors [44]. Halabian et al. [45] combined FE analysis with experimental measurements of needle insertion in the femoral vein catheterization to study the association of the pain score in the patients with the strain and stress distribution around the insertion point. The effect of the insertion angle on the pain score was studied to determine the most appropriate angle for injection. They modelled a part of the skin with subcutaneous tissue (i.e., fat, muscle, and ligament) and femoral artery, in a rectangular cube of the femur tissue adopted from another study by Miller et al. [46]. Figure 4a shows the needle and femur tissue geometry and mesh. In their model, two distinct geometries consisting of the central part and peripheral part were combined, tied together at their interfaces, and were meshed with hexagonal and sweep elements, respectively. Also, a bevel-tipped needle with a cutting angle of 45° was considered in their simulation. Needle's Degrees of Freedom (DOFs) were all constrained except translation along the insertion trajectory and the soft tissue was modelled as an incompressible elastic material. Figure 4b shows

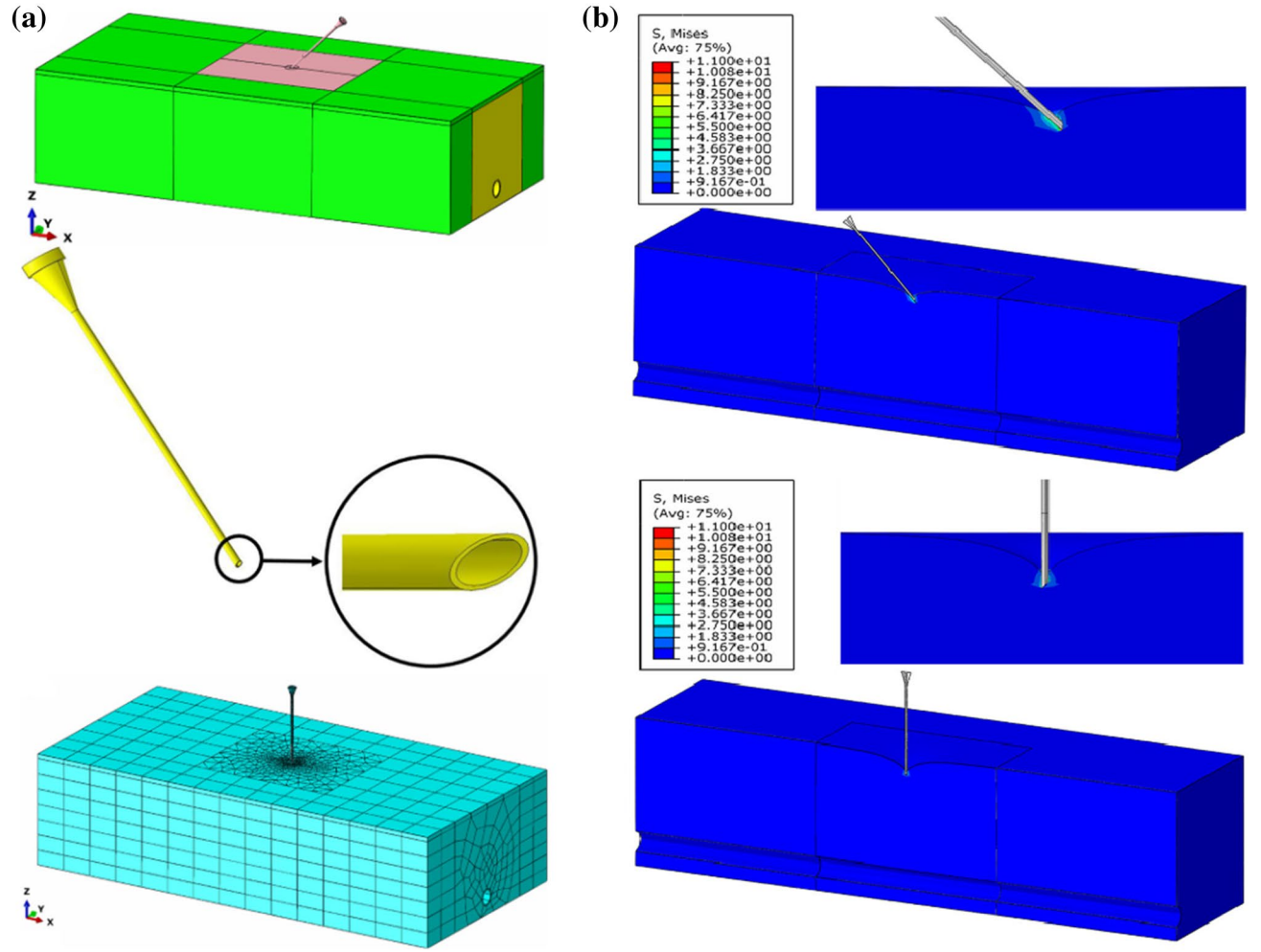

Fig. 4 FE model of needle and femur tissue with no damage mechanism incorporated to the tissue, Reprinted from [45] with permission from Springer Nature: **a** geometry (top) and meshing (bottom) of the 3D model of needle-tissue interaction, **b** the distribution of von Mises stress around the needle-tissue interaction location with an insertion angle of 45° (top) and 90°(bottom)

the distribution of von Mises stress around the needle-tissue interaction area with two of the investigated insertion angles; i.e., 45° (top) and 90° (bottom). The maximum and minimum stress magnitudes around the needle tip occur with the insertion angle of 45° and 90°, respectively. This can be related to the higher level of shear stress in the tissue with the insertion angle of 45° that and that the shear stress is the dominant stress component compared to the normal stress in this particular case. As they did not define any damage mechanism in their model, no rupture was envisaged to occur during the insertion procedure, and the needle did not penetrate the deep parts of the tissue. Amin et al. [47] also analyzed needle insertion into the skin for insulin therapy using FE simulation and studied the effects of insertion angles and needle lengths on the patient injury and pain in terms of the maximum stress and strain values around the insertion point. A Computerized Tomography (CT) image dataset of the healthy abdominal skin was used to reconstruct the model [48] and a bevel-tipped needle was considered. All FE simulations were performed using MSC Marc. Similar to Halabian et al. [45] the needle tip was inserted into the skin without considering any damage mechanism in their model.

The geometry and dimension considerations of microneedles play an important role in their applicability and effectiveness. Loizidou et al. [49] exploited CT scan imaging and FE analysis to study the effect of the geometric composition of microneedles on their mechanical strength and skin-penetration characteristics. They investigated an array of 3×3 microneedles with three different base geometries for microneedles including triangular, square, and hexagonal. Microneedles were made of poly-lactic-co-glycolic acid (PLGA) material which was considered linear elastic. Also, the skin was modelled as a two-layer cylindrical structure, emulating stratum corneum and viable epidermis (top layer) and the dermis (bottom layer). Both epidermis and dermis were simulated as nearly incompressible linear

elastic materials. They assessed von Mises stress and critical buckling loading for different geometries of microneedles. Figure 5 shows the buckling modes (a) and surface von Mises stress (b) on an array of microneedles with a triangular-shaped base. Based on their observation, hexagonal and square base microneedle arrays had analogous buckling modes and stress distribution in which the failure point was located slightly above the microneedle tip.

Radhika and Gnanavel [50] employed FE analysis to investigate the efficiency of various polymer-based microneedles during the insertion process into the porcine skin. They compared the numerical results of exerted insertion force as well as the insertion depth of two polymers, polycarbonate (PC) and polyurethane (PU), with silicon. Figure 6-a and Fig. 6-b compare the penetration performance of two types of microneedles (silicon and PC) into the skin in terms of microneedles deformation and von Mises stress, respectively. Their results showed that the deformation of silicon microneedle was almost twice the deformation of PC microneedle, while the stress concentration on PC microneedle was much larger than that on silicon microneedle. They did not provide material failure criteria, but they reported that PU material structurally failed during the insertion process and only PC could cope with the maximum load of 40N. They compared their numerical results with the experimental results just for PC (insertion depth vs force) with a deviation of 18.17%.

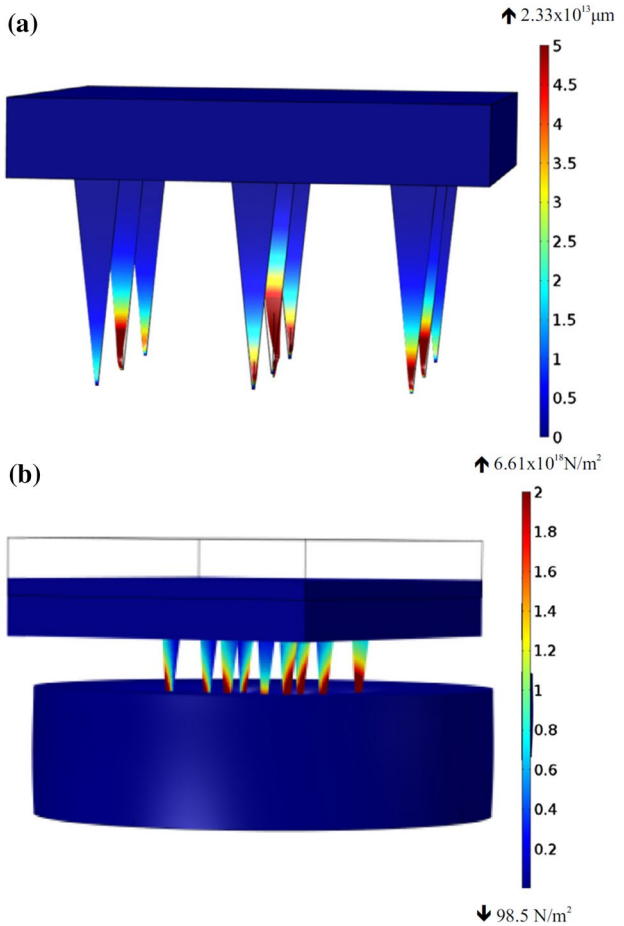

Fig. 5 Results of FE modelling interaction of a 3×3 microneedle patch with porcine skin while no damage mechanism was implemented in the tissue, Reprinted from [49] with permission from Elsevier: **a** buckling modes, **b** and the distribution of surface von Mises stress

The investigation of needle-tissue interactions using non-invasive FE models can provide lots of information about the deformational behaviour of soft tissues and their stress–strain characteristics. Moreover, these models are usually computationally less expensive than invasive models, and easier to be conducted on various biological tissues, with complicated geometrical and mechanical properties. It is usually achievable to incorporate different types of hyperelastic and viscoelastic properties to the tissue in these models, while they still work efficiently and with lower odds of divergence issues compared to more complicated models incorporating damage mechanisms for the soft tissue. However, the information obtained from these models is usually limited and cannot be applied to all needle insertion procedures, especially for high strain rates in which crack propagates rapidly in the tissue, or for analyzing medical cases in which needle penetration into the depth of the tissue is necessary. For this reason, invasive FE models play very important roles in studies dealing with needle-tissue interaction.

3 Invasive Finite-Element Models

Although non-invasive needle-tissue interaction models provide remarkable information about the tissue and needle interaction, most medical applications involve tissue puncture and crack propagation. Therefore, modelling the needle insertion into soft tissues enabled by implementing different damage mechanisms in FE method was investigated by many groups in recent decades. We classified the studies of invasive FE models into five categories, namely nodal separation, element failure/deletion, cohesive zone (CZ), arbitrary Lagrangian–Eulerian (ALE), and coupled Eulerian–Lagrangian (CEL) methods, which will be discussed separately in detail. In addition to providing the detailed FE modelling techniques and the main insightful results, that can help the reader to deal with different modelling challenges, we summarized the main advantages and disadvantages of each method at the end of the related sections. These can be beneficial to guide choosing the appropriate method for future modelling studies.

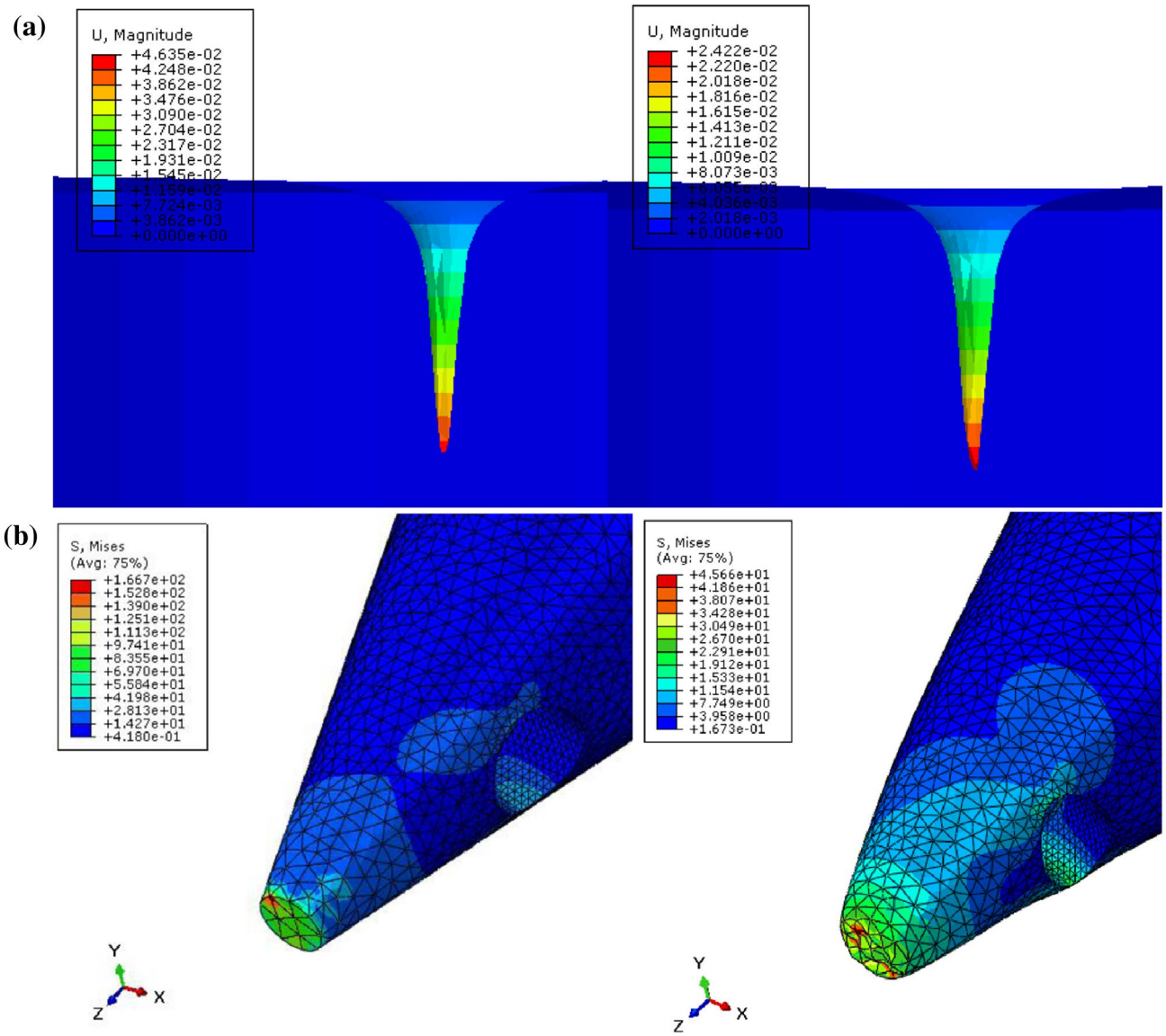

Fig. 6 Results of FE modelling of microneedle-porcine skin interactions without incorporation of any damage mechanism in the tissue, Reprinted from [50] with permission from Elsevier: **a** deformation of silicone microneedle (left) compared to the deformation of polycarbonate microneedle (right), **b** von Mises stress on silicon microneedle (left) compared to von Mises stress on polycarbonate microneedle (right)

3.1 Nodal Separation Models

Some studies in the literature defined the damage mechanism using algorithms based on the displacement of nodes in the cutting zone; hence we call them nodal separation models. Although a damage mechanism is included in these models, it is not established based on a failure mechanism in elements throughout the model or even elements located in the cutting zone. Instead, these models exploit parameters such as local effective modulus (LEM) or fracture toughness to calculate the cutting force as the cutting edge advances. The needle insertion iteratively progresses the procedure until the target insertion depth is achieved. Chanthasopeenphan et al. [51, 52] modelled the cutting process of the liver tissue based on a sequence of intermittent localized crack extensions. Each of the localized crack extensions was realized by applying a localized linear force–displacement loading followed by sudden unloading. They used ex vivo experimental data of cutting the pig liver to find the self-consistent local effective modulus of elasticity for each specimen. Based on the liver specimens' thickness, they used a three-dimensional model as well as two-dimensional models with plane-stress and plane-strain elements. They calibrated LEM to reproduce the experimental cutting force during the

cutting procedure. Local force increments were divided by displacement increments at various depths of insertion to calculate LEM and to tune the corresponding elastic moduli. As the cutting edge advances, the nodes in front of it are pushed and united sequentially. Therefore, instead of incorporating element failure, the cutting force was idealized to solely cause elastic deformation in the tissue. Although their model can be considered superior in terms of computational cost, it is not flexible enough to be used for various cutting tools, speeds, and tissues.

Gokgol et al. [53] carried out several experiments of inserting custom-made needles into bovine livers and developed an FE model based on their experiments. They chose a hyper-viscoelastic material model for the bovine liver tissue and estimated the material properties using static indentation and ramp-and-hold experiments. An energy-based fracture mechanics approach was used to define crack propagation in the tissue. They developed a simplified two-dimensional FE model that contained only the region around the needle insertion point and the solution was considered to be axisymmetric with respect to the insertion axis. Figure 7a shows their model with two different needles: a cylindrical probe with a round tip (left), and a needle with a sharp tip (right). They used an inverse solution to optimize the liver mechanical properties by minimizing the error between simulation and experimental force responses during the needle insertion in a displacement-controlled simulation. A 5-term Mooney-Rivlin strain energy function was used to define the hyperelastic properties of the tissue and a generalized Maxwell solid model was employed to characterize its viscoelastic properties. The node separation at the needle tip was defined based on the comparison of viscoelastic work and fracture work during the insertion process. To this end, the fracture work was calculated by multiplying the crack area by the tissue fracture toughness and the viscoelastic work was obtained by calculating the difference between the total work and fracture work. The viscoelastic work exceeding the fracture work led to the separation of the next node and one-step penetration of the needle into the tissue. They defined the contact between the needle and the tissue by a trial-and-error identification on three parameters including the coefficient of friction, normal penalty stiffness factor, and penetration tolerance factor. The distribution of von Mises stress around the probe/needle is shown in Fig. 7b for the cylindrical probe (left) and the sharp needle (right). The maximum stress values in the tissue were approximately similar in the two cases. However, when the probe was inserted into the tissue, a larger part of the tissue tolerated a high amount of stress compared to the insertion of the sharp needle in which only a tiny zone of tissue bore the same level of stress.

Wang et al. [54] simulated the interaction of flexible needles with soft tissues using an FE coupling model in

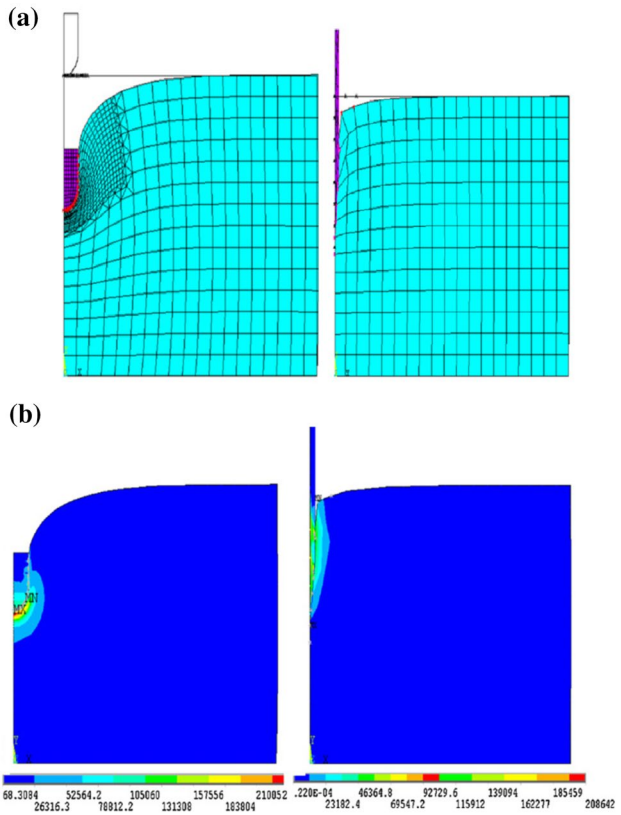

Fig. 7 FE modelling of needle insertion into bovine liver using a nodal separation model, Reprinted from [53] with permission from Elsevier: **a** geometry and mesh configuration for a cylindrical probe with a round tip (left) a needle with a sharp tip (right), **b** bovine liver deformation results for the cylindrical probe (left) and the sharp needle (right)

ABAQUS to calculate the tissue deformation, needle deflection, and bending angle during the insertion process. To this end, the needle was modelled as a simple cantilever beam and the distribution of force components on it was investigated. The entire needle was discretized to multiple needle segments using beam elements that are connected to each other by one node between two adjacent segments. The FE simulations were carried out using both two-dimensional and three-dimensional models using quasi-static analysis. In the two-dimensional model, the needle did not rotate and therefore its trajectory remained in the same plane during the simulation. In the three-dimensional model, however, the needle can rotate, and the insertion trajectory did not remain parallel to the initial plane of beam elements. To simulate the needle insertion process through static mechanical analysis, the whole process was divided into several steps iteratively based on the needle nodes' displacement. In their modelling strategy, the needle and tissue were analyzed separately, and their interaction was translated into the interaction between needle nodes and soft tissue nodes. Their results showed that the tissue displacement increased with the increase of

insertion depth, and the more needle went inside the tissue, the more its trajectory deviated from its initial trajectory.

Nodal separation FE models are among the invasive models with comparatively lower computational costs, as they do not include complicated elements with a pre-defined failure mechanism. However, they usually require lots of iterations to investigate the needle insertion procedure and to find out the insertion trajectory. These models usually amalgamate the benefits and drawbacks of simple non-invasive models with more complicated invasive models. Hence, in a general statement, they are more computationally expensive than non-invasive models and less expensive than many other invasive models. Moreover, although they can incorporate crack propagation in the tissue, they usually do not have the capability of invasive methods that implement a damage mechanism to the model's elements directly.

3.2 Element Failure/Deletion

Since in invasive models, the needle can penetrate the tissue, an algorithm is required to emulate the cutting procedure while maintaining the contact between the needle and tissue. In FE models, element failure and element deletion approaches are among the most prevalent ones that can emulate invasive cutting procedures while maintaining the needle-tissue contact. In these approaches, a damage model based on von Mises stress failure, ultimate strength, Johnson–Cook damage, shear strain threshold, distortion energy failure, etc. is adopted to enable cutting the tissue. Unlike nodal separation models, here we deal with damage mechanisms incorporated directly into the elements that constitute the tissue. Damage is set up either on the whole tissue domain or on the cutting zone where the needle directly interacts with the tissue.

Kong et al. [55] presented an FE model of microneedle insertion into a multilayer skin consisting of stratum corneum, dermis, and hypodermis using ABAQUS/Explicit solver, based on the effective stress failure criterion and element deletion technique. They validated their model using the experimental data obtained by Davis et al. [56] and employed their model to investigate the effect of microneedle geometry on the insertion force. They modelled stratum corneum and dermis layers with an isotropic incompressible hyperelastic material characterized by the one-term Neo-Hookean strain energy function while modelled the hypodermis layer as a linear elastic material. The mechanical properties were chosen based on the experimental data reported by Wildnauer et al. [57], Duck [58], and Gerling and Thomas [59] for stratum corneum, dermis, and hypodermis layers, respectively. In their model, the hypodermis layer was not involved in the failure process and the microneedle could only penetrate the upper surface of the dermis layer. The simulations were performed using an axisymmetric model and meshed with four-node CAX4R elements. Only a limited part of the skin around the insertion point, big enough to avoid the effect of boundaries on the penetration zone, was considered in their model. The microneedle was modelled as a rigid body and the interaction of the microneedle tip and the skin was defined based on the surface-to-surface contact using a kinematic contact algorithm. The crack propagation was captured using an element-deletion algorithm implemented in a material subroutine with a von Mises stress failure criterion. The whole process was quasi-static.

Chen et al. [60] employed a non-linear FE model using the micro-biomechanical properties of the skin to investigate microneedle insertion. They investigated the skin deformation during the insertion process as well as the force response of the microneedle versus its displacement. They also provided some information on the effect of geometrical parameters of the microneedle on its fracture. They modelled skin as a multilayer tissue consisting of stratum corneum, viable epidermis, dermis, and hypodermis layers with thickness values of 20 µm, 80 µm, 1 mm, and 1 mm, respectively. They exploited the first-order Ogden hyperelastic material model for stratum corneum, viable epidermis, and dermis, while modelled the hypodermis layer as a linear elastic material. In order to avoid the effect of boundaries on the insertion process, they considered a large skin region, which was 20 times larger than the microneedle. The microneedle was defined as a rigid body in their model. Both microneedle and skin tissue were meshed with Ansys SOLID164 elements. An element-deletion damage model based on the ultimate strength of each element was implemented to enable microneedle penetration into the skin tissue. They defined an eroding surface-to-surface contact model that maintained the needle contact with interior elements (i.e., elements beneath the elements that form the exterior surface of the tissue) after the deletion of exterior elements (i.e., elements which form the exterior surface of the tissue). Their results showed that as soon as the microneedle touched the skin surface, it started to deform the skin tissue and increased the effective stress in it by moving forward gradually. The maximum von Mises stress occurred on the surface of the skin tissue around the microneedle tip, and the separation of the skin elements occurred when the failure criterion was satisfied.

Assaad et al. [61] studied the insertion of a bevel-tipped needle into a soft gel using a combination of the Johnson–Cook damage model [62] for the damage initiation and an element deletion-based method for the damage evolution during the simulation. The damage model for fracture strain (ε^f) was defined by [62]:

$$\varepsilon^f = \left[D_1 + D_2 e^{-D_3 \sigma^*}\right]\left[1 + D_4 ln\dot{\varepsilon}^*\right]\left[1 + D_5 T^*\right] \tag{5}$$

where D_1, D_2, D_3, D_4, and D_5 are material constants. Also, σ^*, $\dot{\varepsilon}^*$, and T^* are pressure-stress ratio, dimensionless plastic strain rate, and homologous temperature of the gel, respectively. These parameters can be found by $\sigma^* = \frac{\sigma_m}{\bar{\sigma}}$, $\dot{\varepsilon}^* = \frac{\dot{\varepsilon}}{\dot{\varepsilon}_0}$,

and $T^* = \frac{T}{T_m}$, where σ_m and $\tilde{\sigma}$ are hydrostatic pressure and von Mises stress, $\dot{\epsilon}$ is strain rate for $\dot{\epsilon}_0 = 1.0\frac{1}{s}$, and T and T_m are the gel temperature at the start of the experiment and the melting point temperature of the gel, respectively. They calculated the damage constants based on a compression test on the gel and verified their simulations using their experimental data of in situ images of the gel rupture. The gel was modelled as a linear elastic material in ABAQUS/Explicit solver, the needle and gel were both meshed using eight-node brick elements, and the gel was partitioned to reduce the number of DOFs and the computation time.

Peng et al. [63] used a failure criterion based on the distortion energy theory to model needle insertion into the cornea. The cornea was simplified to two layers including epithelium and stroma, which were defined as hyper-viscoelastic materials. They studied the needle insertion force at different insertion speeds and investigated the tissue injury using the von Mises stress around the insertion point. Since the properties of the two orthogonal directions in the cornea are almost the same [64, 65], it was modelled in an axisymmetric configuration in their model. The cornea was constrained by sclera which was simplified as an elastomer. They used four-node bilinear axisymmetric quadrilateral elements (ABAQUS CAX4R) and implemented reduced integration, distortion control, and enhanced hourglass control. The contact between the needle and tissue was defined by surface-to-surface explicit contact using a penalty contact algorithm with a sliding formulation and the normal behaviour of a hard contact definition (i.e., any contact pressure in two involved surfaces can be transferred between them and if the pressure reduces to zero they separate). Also, the tangential friction behaviour was related to the viscosity of the tissue that changed with the insertion speed based on the modified Karnopp friction model. They implemented a failure criterion using element deletion by defining a state variable, δ, in which the yield condition for material failure was expressed as:

$$\delta = \sqrt{\frac{1}{2}[(\sigma_1 - \sigma_2)^2 + (\sigma_2 - \sigma_3)^2 + (\sigma_3 - \sigma_1)^2]} \leq [\sigma] \quad (6)$$

where σ_1, σ_2, and σ_3 are the three principal stresses, and σ is the breaking strength. Their results showed that the needle successively punctured epithelium, stroma, and then the lower surface of the cornea. During this procedure, the von Mises stress suddenly increased with the insertion of the needle into the corneal epithelium and then remained at an almost constant level during the rest of the insertion procedure.

Singh et al. [66] introduced a three-dimensional FE model of the insertion of flexible neural probes made with SU-8, Parylene C, or Polymer Shank. The probes can be used for signal acquisition devices like brain-to-computer interface systems. They also performed several experimental measurements on agarose tissue phantom, ex vivo rat brain, and ex vivo chick embryonic brain tissues to validate their FE models. They modelled agarose and the brain tissue as Ogden hyperelastic material with the parameters introduced in [67, 68]. The tissue and probe were meshed with eight-node reduced-integration (C3D8R) elements. The simulations were performed using ABAQUS/Explicit dynamic solver. An element failure approach based on the shear strain threshold was incorporated to enable probe insertion into the tissue. They performed sensitivity analysis on various geometrical and material properties. Jiang et al. [69] developed a three-dimensional FE model to simulate hollow needle insertion into the skin and investigated the effects of the needle diameter, tip angle, and insertion speed on the penetration force and stress and strain values around the insertion point. They assumed the needle to be rigid and used the mechanical properties of medical silicone, which was previously shown to have similar properties to the human skin [70]. They used hexahedral elements and considered a bilinear elastoplastic and strain-failure behaviour for the tissue. Figure 8-a shows the model of the needle insertion into a cylindrical shape structure, which represents the skin in their modelling configuration. The contact between the needle and tissue was of face penetration type with the Coulomb friction law. The whole simulation procedure was conducted through 40 incremental steps solved by the Full Newton–Raphson iterative method. They simulated both insertion and extraction of the needle. Figure 8-b shows the calculated von Mises stress and maximum principal strain distributions in the skin tissue in several steps of their simulation including insertion, maximum depth, and extraction stages of the process. During the whole procedure, the maximum stress and strain values occurred around the needle tip. Initially, with the insertion of the needle, the stress and strain increased with the increase of puncture depth and then decreased rapidly as the needle was pulled.

In reality, when the tissue is cut, no part of it will be removed or completely diminished, but in models, that are based on element deletion, some parts of the tissue get deteriorated and removed during the simulation. However, these models can still be considered valid and even more realistic than many of other models because they can inherently incorporate a practical crack propagation mechanism in the tissue very similar to reality, especially when the elements in the vicinity of crack propagation are small enough so that effects of their deletion on the simulation are negligible. These models are usually dependent on the mesh size around the crack front and a mesh study is required to make sure the effect of elements' size on the final results is negligible. One important strength of these models for modelling different types of soft tissues is the diversity of damage mechanisms that can be applied to the model elements. It also gives

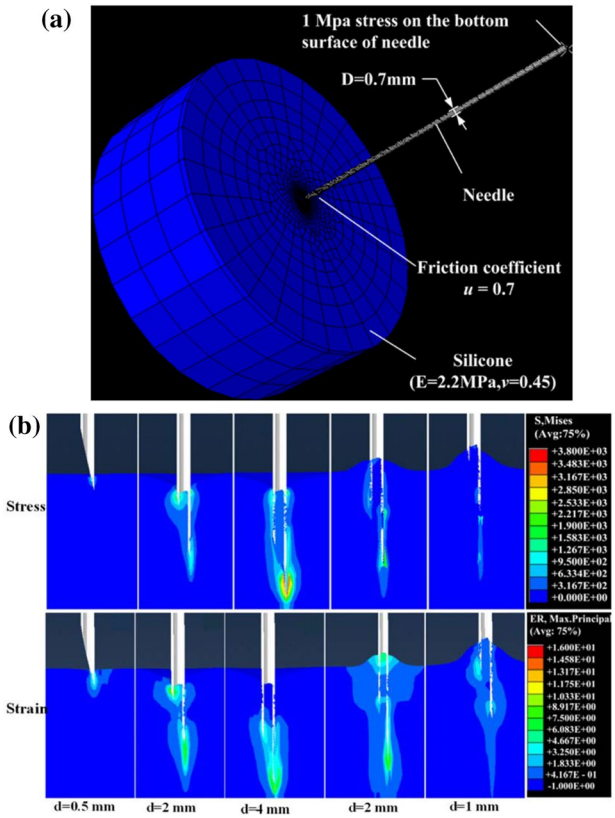

Fig. 8 FE modelling of needle insertion into a limited part of skin tissue using failure strength of the tissue [69]: **a** 3D geometry and mesh configuration, **b** stress and strain fields in the skin in different stages of insertion and extraction of the needle

researchers multiple choices in terms of how to implement the best damage mechanism for the tissue or which existing implementation in FE packages to choose for modelling the needle insertion process.

3.3 Cohesive Zone Method

The cohesive zone method (CZM) is a specific failure mechanism that has been widely used in numerical modelling of crack propagation as it allows the creation of crack surfaces during the simulation [71, 72]. For the definition of the cohesive zone, a traction–separation law (TSL) [73] should be used that relates the cohesive traction vector to the separation vector across the cohesive surfaces. All models in the literature, that exploited CZM for needle insertion into tissue, chose a bilinear TSL (Fig. 9a) to relate the cohesive traction (t) and strain (ε). Based on this definition the cohesive traction increases linearly with the increase of distance between cohesive surfaces until a maximum value of t_c, known as failure traction, at which damage of cohesive zone initiates. Hereafter, the cohesive traction decreases linearly with the increase of distance between cohesive surfaces until the cohesive traction diminishes and cohesive surfaces separate completely. Here, we show the separation value at the damage initiation point and ultimate separation length by δ_y and δ_0, respectively. Using the definition of a constitutive thickness parameter (T_c), the linking strain and separation distance (δ) are correlated with each other as [74]:

$$\varepsilon_{n,s} = \frac{\delta_{n,s}}{T_c} \tag{7}$$

where n and s indices represent normal and shear directions, respectively. By setting T_c to unity, the initial cohesive traction can be related to strain/separation with the initial stiffness of (K_i) as follows [74, 75]:

$$\boldsymbol{t} = K_n\varepsilon_n\boldsymbol{e_n} + K_s\varepsilon_s\boldsymbol{e_s} = K_n\delta_n\boldsymbol{e_n} + K_s\delta_s\boldsymbol{e_s} \tag{8}$$

Initially, Misra et al. [75] used CZM in a two-dimensional FE model to investigate needle-tissue interaction forces for bevel-tip needles. They assumed the normal and shear stiffnesses to be equal to each other and equal to the tissue's Young's modulus. They also chose a separation value of $\delta_c = \delta_0 - \delta_y$ equal to the needle diameter and found failure traction (t_c) by knowing the material fracture toughness in terms of the strain energy release rate (G_c) from the following equation:

$$t_c = \frac{2G_c}{\delta_0} \tag{9}$$

They exploited cohesive elements (COH2D4) and a mixture of bulk elements including quadrilateral (CPE4H) and triangular (CPE3H) in their FE model. Furthermore, they studied both phantom tissues (soft and hard plastisol gels) and biological tissues (porcine gel and chicken breast tissue) experimentally to obtain their mechanical properties to be included in modelling. They performed several sensitivity analyses using their FE model to study the effects of tissue fracture toughness, linear and non-linear elasticity, and needle tip bevel angle on the tip forces.

Although using bilinear TSL is a prevalent approach for the definition of cohesive elements in cutting simulations, it is not always easy to find appropriate parameters for cohesive elements, and experimental studies along with numerous simulations are required to find the best fit. Oldfield et al. [74] developed an experimentally validated two-dimensional FE model of needle insertion into soft tissue phantoms using zero-thickness cohesive elements to enable crack propagation in the tissue. A bilinear TSL was considered for the definition of the cohesive zone in their model and multiple simulations with various cohesive parameter values (1 mm $\leq \delta_y \leq$ 7 mm and 1.5 mm $\leq \delta_0 \leq$ 7.5 mm) were taken into account. They provided

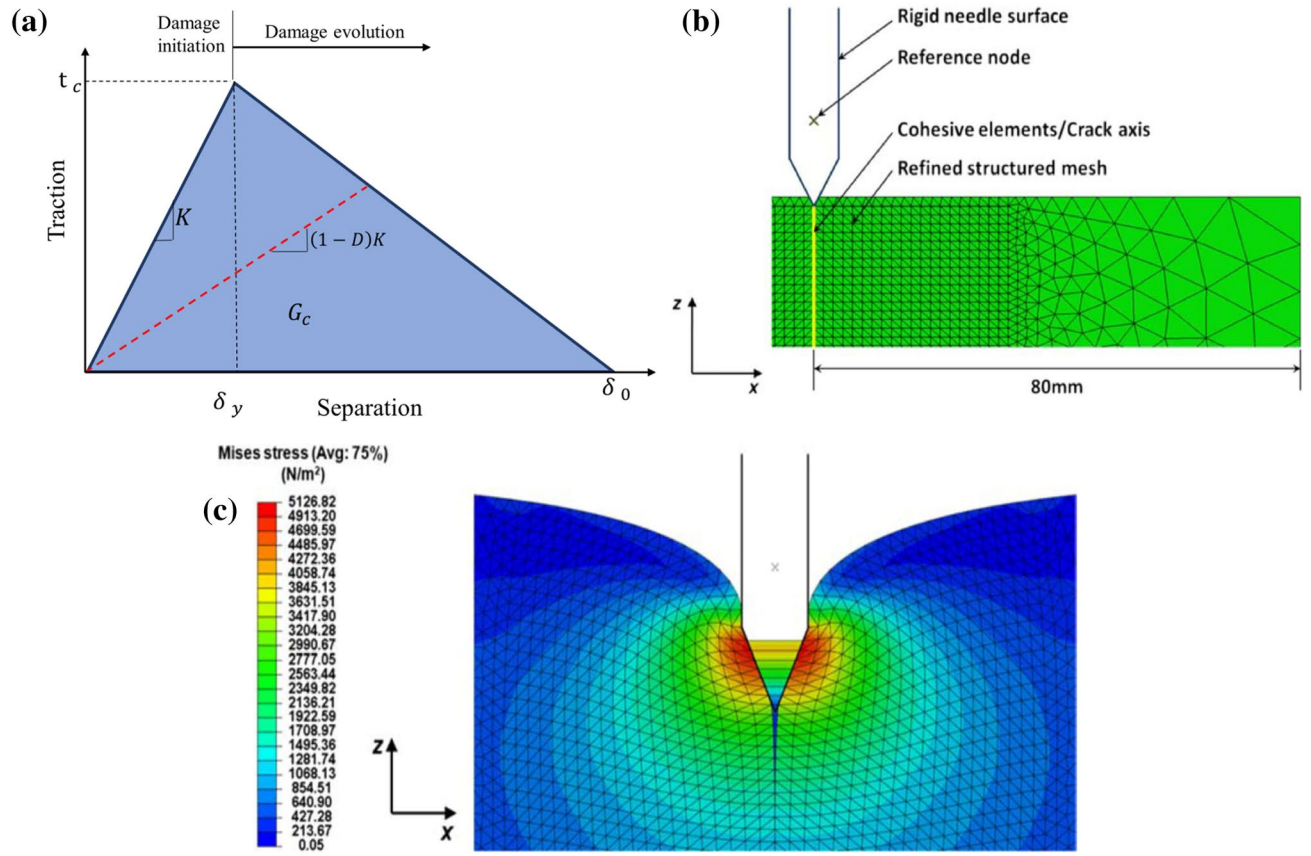

Fig. 9 FE modelling of needle insertion into a gelatine tissue phantom using CZM: **a** bilinear traction–separation law, **b** 2D model of through-and-through penetration of needle into the tissue, Reprinted from [74] with permission from Taylor and Francis, **c** stress and element distortion prior to the failure of the first cohesive element during the insertion of needle into the tissue, Reprinted from [74] with permission from Taylor and Francis

force–displacement results for the investigated variation of cohesive parameters as well as a detailed interpretation of different stages of the insertion procedure and the related energy distribution of the cutting process. They stated that the energy required for needle insertion (W_{ext}) consists of three main components including strain energy (U_s), fracture energy (U_G), and frictional energy (U_f) [70, 76]:

$$W_{ext} = U_s + U_G + U_f \tag{10}$$

A simple two-dimensional model of tissue deformation was suggested to determine the work required for tissue deformation (equivalent to the strain energy component) during the needle insertion, whereas a more complicated two-dimensional plane strain model was introduced to investigate the insertion process that includes all energy components together. Figure 9b depicts the mesh configuration of their proposed model. The needle was modelled as a rigid body and a reference node, whereas an elastic material model was chosen for the gelatin block. The gelatin block was meshed using three-node plane strain elements while the cohesive zone was meshed with four-node plane strain cohesive elements. The interaction between the gelatin block and the needle was modelled using a penalty contact algorithm with either frictionless contact or frictional contact defined using the Coulomb friction law. Figure 9c shows the von Mises stress distribution in the cohesive zone and its surrounding area in the tissue prior to the failure of the first cohesive element. In this stage of insertion, the material starts to deform remarkably and the FE might need adaptive meshing techniques, especially if frictional forces are included in the model. The needle insertion was once simulated without considering cohesive elements and again by adding the cohesive elements to the final model. Their results show a significant reduction in the stress level happened with omitting the cohesive elements. Furthermore, the gelatin elements did not maintain their contact with the needle completely when the cohesive elements were removed.

Oldfield et al. [77] also used their previously proposed model to investigate the effect of blade insertion rate on the strain energy release rate, contact interactions, and deformation in a gelatin soft tissue phantom. They considered

the insertion rate to be in the range of 0.25–2 mm/s. In their study, they exploited a combination of experimental measurements and FE simulations. They modelled the tissue and blade geometry symmetrical, used linear triangular elements and cohesive elements, and performed the simulations using an explicit solver. Gelatin was modelled as a viscoelastic material reported in the literature [35]. Similar to their previous study, they defined cohesive zone using a bilinear traction–separation law. They also applied a small amount of stiffness-proportional damping to prevent large oscillations in the force–displacement results.

The geometrical complexity of the cutting edges of needles urges on using three-dimensional FE models that can accurately capture the cutting process considering the exact shape of the needle tip and its effects on the stress distribution in the tissue and needle reaction force. Unlike previous studies, Tai et al. [78] implemented the CZM in a three-dimensional FE model to simulate the insertion of hollow needles with different geometrical shapes into a soft polyvinyl chloride (PVC) phantom. In their model, the cohesive strength (or fracture strength, t_c) was calculated from the fracture toughness (K_{IC}) and collinear crack of half-width (a_0) by [78]:

$$t_c = \frac{K_{IC}}{\sqrt{\pi a_0}} \tag{11}$$

They also considered the initial stiffness as [79]:

$$K = \frac{10E}{d} \tag{12}$$

where E is bulk elasticity and d is the maximum element size. They defined the needle as a rigid body using shell elements. They showed if a thin layer of the tissue is considered in the model, applying an excessive needle motion leads to extreme deformation of the tissue that distorts the pre-defined CZ region and obviates successful insertion modelling. Because increasing the thickness of the tissue, considered in the model, increased the computational time substantially, they instead defined an alternative virtual material to support the primary tissue. This virtual material had a much coarser mesh and without any failure criteria and interaction with the needle. In their study, all simulations were conducted under a quasi-static condition using ABAQUS/ Explicit solver. Using their FE model, they studied needles with lancet and bias bevel tips and compared their axial insertion forces. Their results showed that for the bias bevel needle, the crack propagates exactly on the pre-defined CZ until a transition point in which the cutting edge can no longer split the material. For the lancet tip, this transition happens earlier than that of the bias bevel needle with more distortion of elements in the tissue.

Some applications require steerable needle insertion into the tissue. Since in these applications the direction of insertion and crack propagation in the tissue is usually unknown and unstable, Terzano et al. [80] proposed an adaptive two-dimensional plane strain FE algorithm for needle penetration in gelatin material using the CZM without a predetermined crack propagation trajectory. They exploited the distribution of strain energy density around the crack tip to determine the direction of crack propagation. The tissue was modelled in ABAQUS employing linear triangular elements (CPE3) with a special ring of elements around the crack tip and zero-thickness four-node cohesive elements (COH2D4) with a bilinear TSL along the crack propagation trajectory. Figure 10a and b show the initial configuration of their model geometry and mesh for two different types of needles, respectively. The contact between the needle and tissue was defined using the Lagrange multipliers method with a frictional interaction based on the Coulomb frictional law. The crack propagation was achieved step by step in their model through an iterative algorithm performed with a remeshing strategy carried out by the mesh generator DistMesh in MATLAB [81]. In order to determine the direction of crack propagation, they introduced a fracture criterion based on crack-tip opening displacement and employed a kinking criterion based on minimum strain energy density. Using this approach, kinking angle (θ_c) can be calculated by determining the direction that minimizes the strain energy density (U_s):

$$U_s = \begin{cases} \left(\frac{dU_S}{d\theta}\right)_{\theta=\theta_c} = 0 \\ \left(\frac{d^2U_S}{d\theta^2}\right)_{\theta=\theta_c} \geq 0 \end{cases} \tag{13}$$

Figure 10c shows the inserted needle in the tissue after several crack-propagation iterations. They showed that the trajectory of needle insertion and force–displacement plots depend on the needle tip geometry and the relative stiffness of the needle and tissue.

Finding a validated cohesive model, especially in multilayer biological structures such as the human skin with multiple unknown parameters is another challenge of using CZM [82]. Mohammadi et al. [83] introduced an optimization algorithm to implement a two-dimensional validated FE model for needle insertion into the human skin (Fig. 11a). The skin was modelled as a first-order Ogden hyperelastic material while the subcutaneous fat layer was defined as a simple linear elastic material model. The needle was considered to be rigid. The contact between the needle and skin tissue was defined as a hard contact with Coulomb friction, and a tangential traction with the penalty contact algorithm was applied to model their interaction. They used a bilinear cohesive FE model for which the cohesive parameters

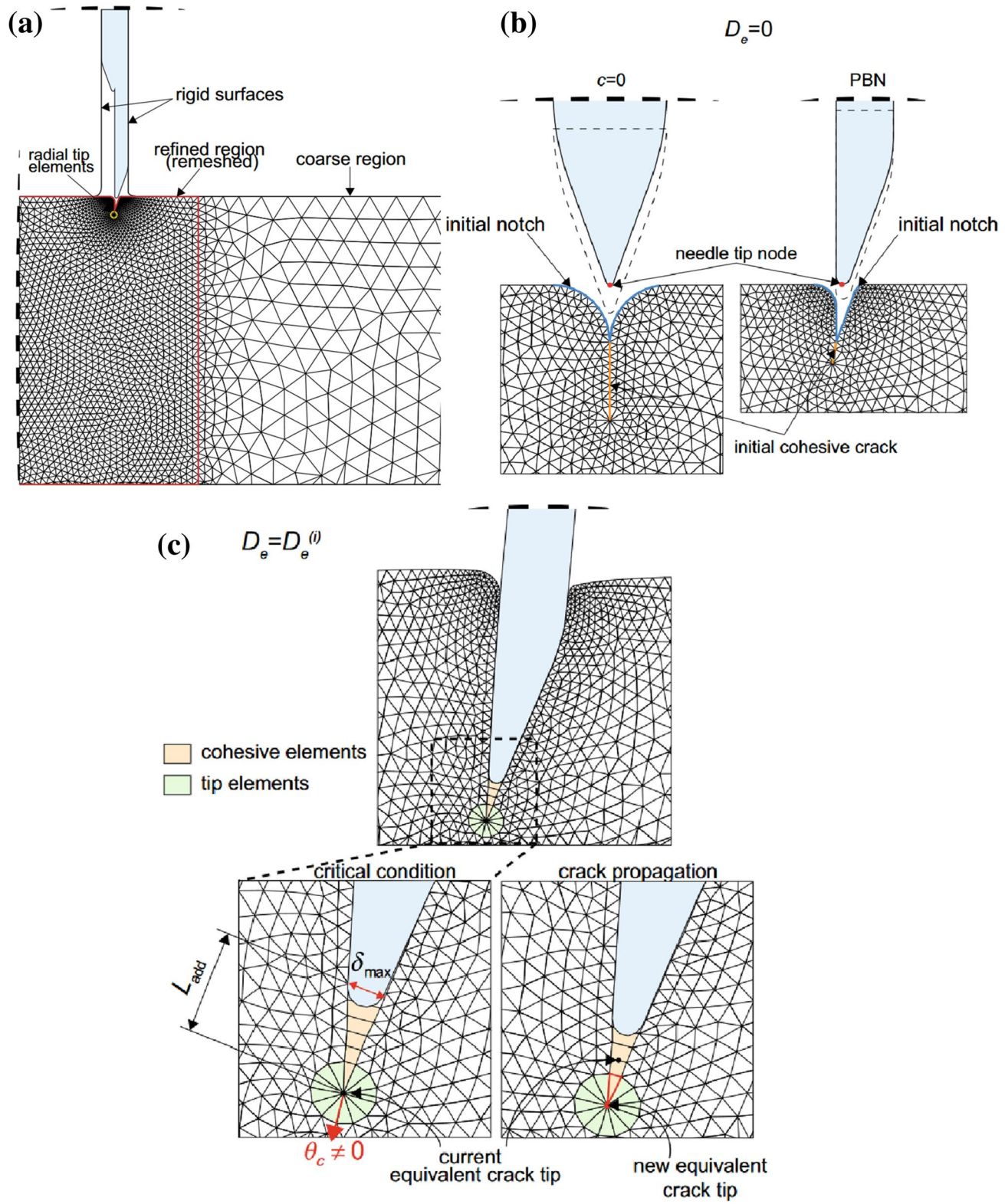

Fig. 10 Adaptive FE modelling of steerable needle insertion into a gelatine tissue phantom using CZM [80]: **a** initial configuration of the model geometry and mesh, **b** detailed view of needle tip and surrounding tissue elements for two different needles, **c** deformed mesh after needle penetration into the tissue

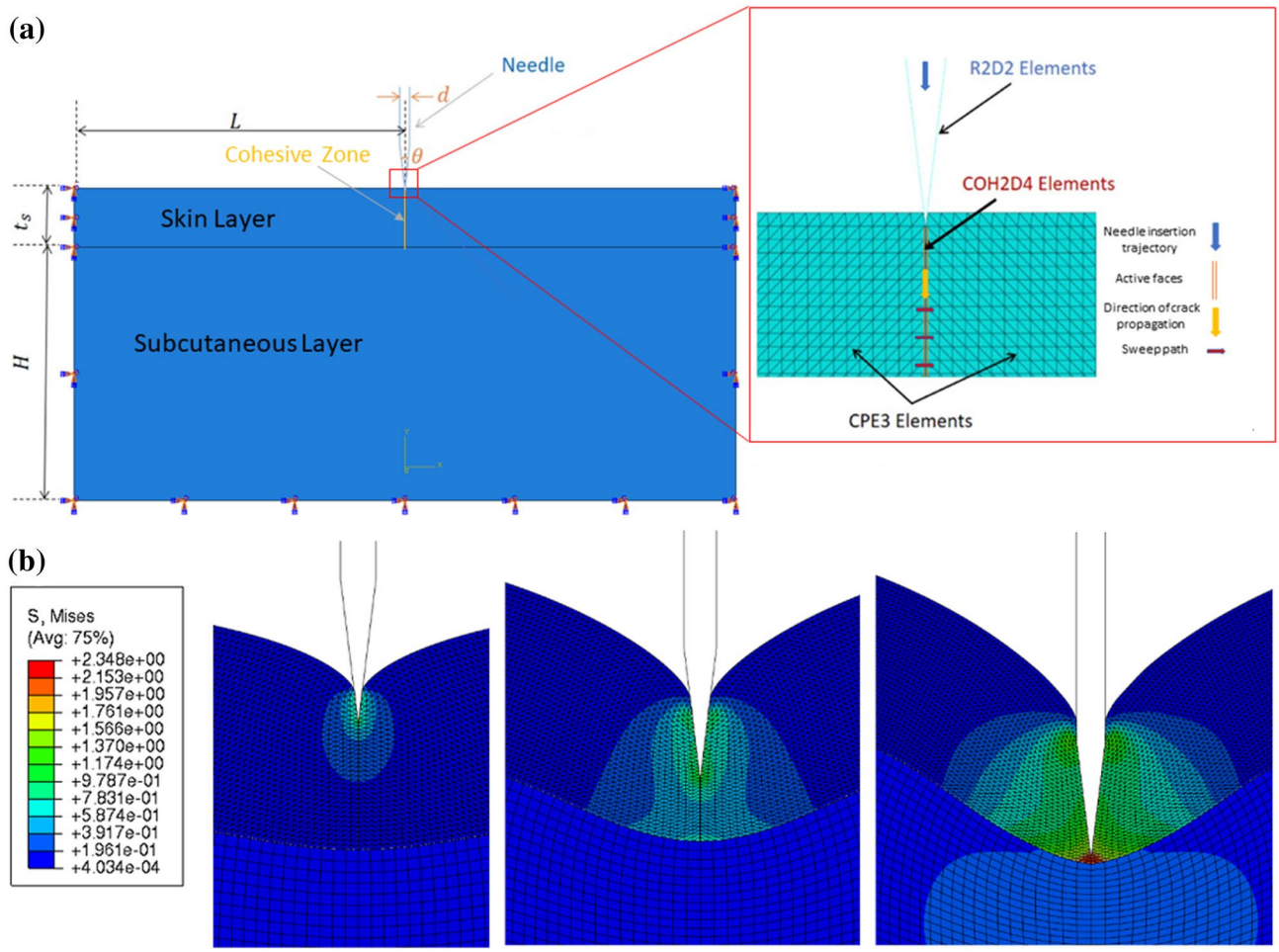

Fig. 11 FE modelling of needle insertion into human skin using CZM, Reprinted from [83] with permission from Elsevier: **a** 2D model consisting of a rigid needle, hyperelastic skin layer and elastic subcutaneous tissue, **b** von Mises stress distribution around the crack tip in the skin tissue in three different instances of insertion

were chosen based on the best fit to the force–displacement experimental data reported in [70]. In their model, the cohesive elements were defined to fail when reaching the ultimate stress. To maintain tissue connectivity in two-dimensional modelling, the cohesive elements remained in the simulation until the end of the insertion process even after full penetration occurred. After the cohesive elements failed, an updated cohesive stiffness (K_D), dependent on a damage parameter (D), was assigned to them:

$$K_D = (1 - D)K \tag{14}$$

where K is the initial stiffness and D represents the loss in cohesive stiffness during the separation procedure; D is zero until the failure point but after the failure of the elements, it increases with the increase of separation length, meaning that the cohesive stiffness decreases with the increase of separation length. Three error functions were taken into consideration to minimize the FE error at the puncture point, during the post-puncture phase, and finally during the whole insertion process. These error functions were used to optimize the subcutaneous fat layer elasticity, coefficient of friction between the needle and skin, and the cohesive parameters (i.e., t_c, K, δ_0), respectively. Figure 11b shows the von Mises stress distribution around the crack tip at three different instances of the insertion process. With the penetration of the needle tip into the tissue, the stress magnitude increased gradually until the puncture point at which a quick stress increase occurred in the tissue. At this point, the needle started to enter the subcutaneous layer with a sudden drop of von Mises stress. They also performed a detailed parametric study on the effect of needle-skin interactions and the needle geometry on the needle reaction force and the von Mises stress distribution in the tissue. Moreover, they provided an energy analysis to show the evolution of energy components (i.e., frictional dissipation, damage dissipation, and stored strain energy) during the full penetration process.

CZM is an appropriate method to simulate the cutting procedure in soft tissue as it can realistically define a crack path in the model and also adapt to large deformation that usually occurs in soft tissue. However, the cohesive elements should be embedded into the continuum elements to enable the modelling of the cutting process during needle insertion. So, there is a challenge in detecting crack-propagation direction and implementing an appropriate mesh. The current solution as discussed in [80] involves using iterative algorithms that add to the difficulty of performing complicated simulations. On the other hand, it is not easy to incorporate such an algorithm into three-dimensional models or at least it is concomitant with high computational costs and requires numerous iterations to simulate the whole insertion process. However, for the cases in which crack propagation and needle insertion trajectory are straight or predictable, using CZM can be considered a very efficient and expedient option.

3.4 Arbitrary Lagrangian–Eulerian

All methods discussed so far are based on a Lagrangian formulation which is the earliest and the most commonly used formulation for modelling cutting procedures including needle insertion into soft tissues. However, when the material undergoes large deformations, elements suffer from excessive distortion, which results in inaccurate prediction or convergence problems. An intuitive solution for compensating for the element distortion is remeshing—if the mesh is highly distorted, a new mesh will be generated for the deformed tissue and the solution from a lightly distorted mesh will be mapped to the new mesh [84]. Generally, in remeshing algorithms, the topology of the mesh can change each time with the generation of a new mesh. Arbitrary Lagrangian–Eulerian (ALE) formulation is a specific remeshing algorithm in which the topology of mesh will be carried out through the whole simulation procedure using mesh smoothing methods [85, 86]. In fracture analysis of continuum models under large deformations, ALE has been proven to be a reasonable and powerful alternative method for Lagrangian formulations [87]. Yamaguchi et al. [88] proposed a three-dimensional dynamic FE model of copper-made needle insertion into agar gel performed using an ALE method. Their model was validated using the equivalent experimental measurements and used to investigate needle deflection and insertion forces. They implemented the ALE-based FE analysis using ANSYS LS-DYNA. The needle and the agar gel were discretized using rectangular shell elements, and hexahedral solid elements, respectively (Fig. 12a).

Yamaguchi et al. [88] used linear elastic and isotropic elastic–plastic material models for the needle and the agar gel, respectively. For characterization of the mechanical

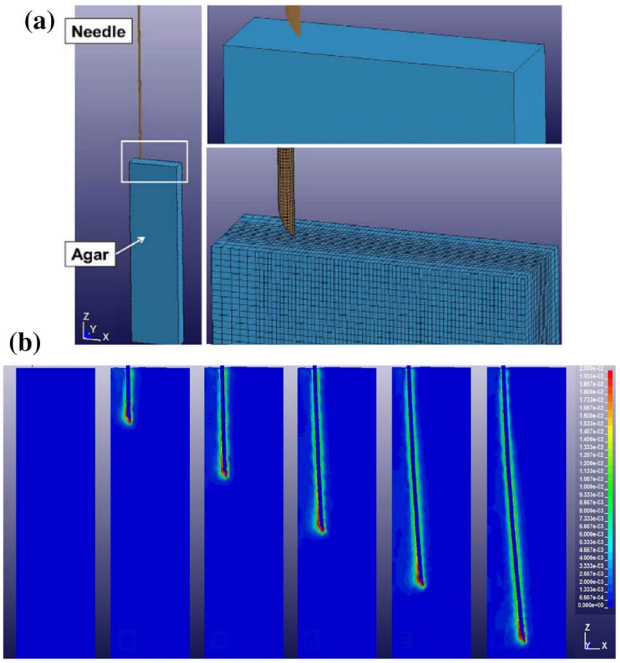

Fig. 12 FE modelling of needle insertion into a soft tissue phantom made of agar gel using ALE, Reprinted from [88] with permission from Elsevier: **a** needle-gel model and its mesh structure, **b** needle deflection and shear stress distribution in different insertion depths

properties of the agar gel, a strain energy function was determined using a three-point bending test. They performed simulations with different angles of the needle tip (i.e., 30°, 45°, and 60°), and their results showed the increase of maximum shear stress with the increase of tip angle. The needle deflection and shear stress distribution in different stages of the insertion process for 30° can be seen in Fig. 12b. For all investigated cases, and in all stages of the insertion process, the maximum shear stress happened in the immediate vicinity of the needle tip. They also compared the experimental and modelling force–displacement results using a two-factor analysis of variance, and provided a force–displacement curve for each bevel angle based on the average experimental results.

Using needles with tiny sizes can lead to complexities like more vulnerability to buckling due to needle slenderness and more computational time owing to the existence of stiff and extremely small solid elements.

Konh et al. [89] proposed novel ALE-based methods to deal with these issues. Figure 13a demonstrates their FE model configurations including the gel and needle mesh and geometry as well as the boundary conditions. They used this model to predict the deflection of a bevel-tip needle inside soft tissue and to investigate the effects of needle diameter and bevel tip angle on the final deformed shape of the needle. Material properties of the soft tissue were considered to be close to those of the prostate properties defined as a

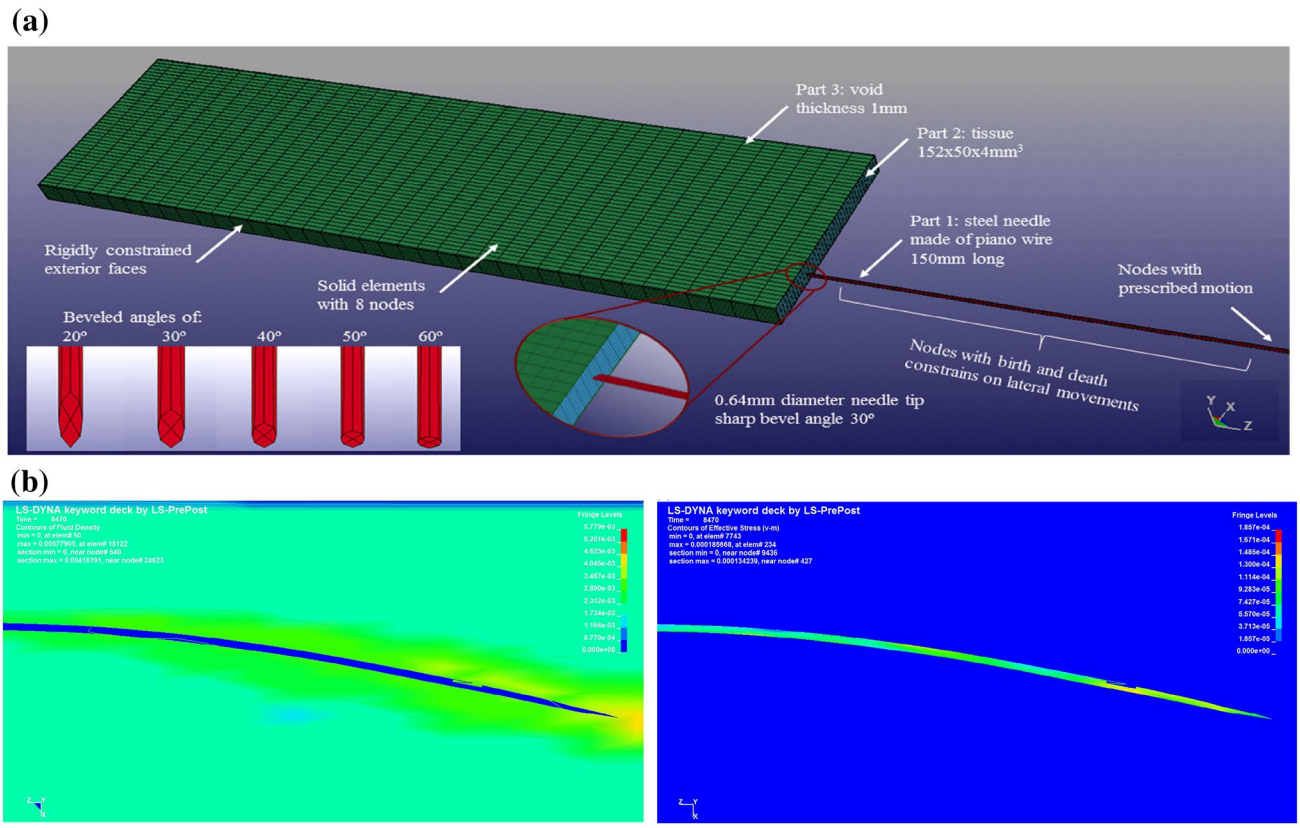

Fig. 13 FE modelling of needle insertion into Plastisol gel using ALE, Reprinted from [89] with permission from Springer Nature: **a** geometry, mesh, and boundary conditions of the model, **b** fluid density contour plot (left) and stress distribution (right) after 150 mm insertion of a needle with a diameter of 0.64 mm into the phantom

linear elastic material. They implemented a fluid–structure formulation in their model in which the solid elements of the needle penetrate the fluid elements of the tissue. Needle-tissue interactions were modelled using a Lagrangian method with a penalty contact algorithm. Tissue elements were defined by ALE elements that allowed flux of material between elements of tissue during the insertion procedure. Eight-node solid elements were considered for both needle and tissue. They also defined a void part surrounding the tissue with similar material properties to the tissue while having no mass to allow tissue mass transfer in the model. Figure 13b shows the distributions of fluid density (left), which indicates the mass of elements per unit volume, and von Mises stress (right) after the 150 mm insertion of a needle with a diameter of 0.64 mm into the phantom tissue. The mass translation between adjacent elements, which was made possible in ALE formulation, is observable in their results for fluid density distribution in the tissue, especially with a remarkable amount around the needle tip. Similarly, the maximum amount of von Mises stress value occurred around the tip of the needle with maximum bending. In their study, the skin puncture was not modelled, and the effect of cutting and frictional forces were assumed to be negligible due to the tiny size of the needles. They also exploited mass scaling and material properties scaling in their model to decrease the computational time. These techniques are based on adding nonphysical mass or material properties like Young's modulus to achieve a larger explicit time-step as much as they do not influence the final results significantly.

Needle coating procedures can change the surface quality of the needle and its interaction with the tissue, and consequently its penetration behaviour in terms of reaction forces, von Mises stress distribution, and needle deflection during the insertion process. Gao et al. [90] investigated the effect of needle surface quality using an experimentally-validated two-dimensional dynamic FE model of fresh porcine loin tissue. The tissue was modelled as a hyperelastic material based on Mooney-Rivlin strain energy density. They simulated the needle insertion process using an explicit solver employing an ALE adaptive mesh. To model the cutting

process, they used surface-to-surface contact based on a kinematic contact algorithm and set fracture strain and displacement at the failure point. Moreover, they implemented the local-mesh refined method in the high-stress and strain gradient zones to achieve a more accurate numerical solution. The needle was considered a flexible body to study its deformation during the insertion process. Two different values for the coefficient of friction between a conventional

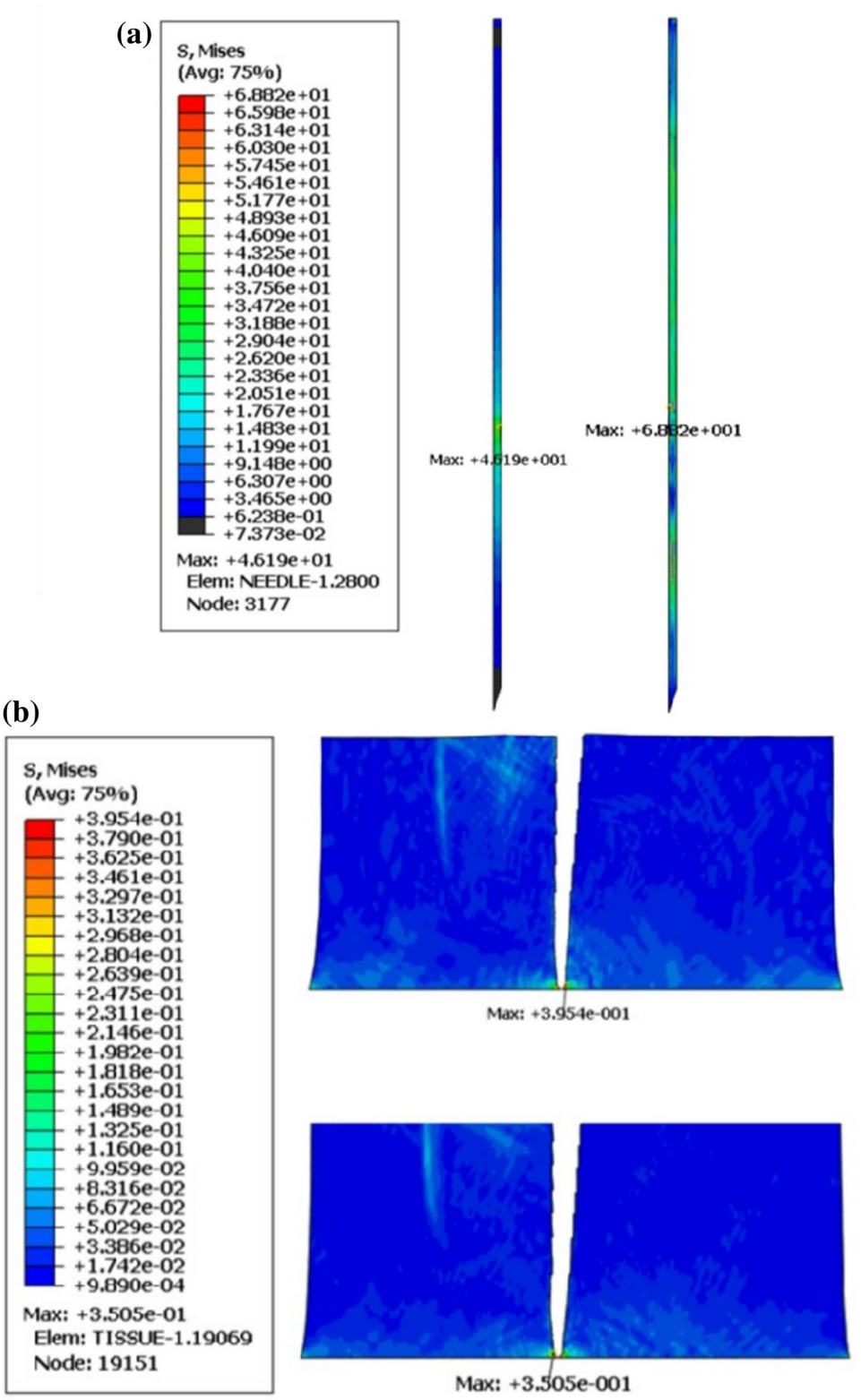

Fig. 14 Results of FE modelling of needle insertion into porcine loin tissue using ALE [90]: **a** von Mises stress in the needle when the force is maximum for coated (left) and uncoated (right) needles, **b** von Mises stress in the tissue when force is maximum using coated (bottom) and uncoated (top) needles

needle and tissue (0.42) and a needle with biocompatible hydrophilic coating and tissue (0.03) were found based on their model. The coating reduced the insertion force and the deformation of the tissue by decreasing friction. Figure 14a and b show von Mises stress distributions during the insertion of both coated and uncoated needles happening in the needle and tissue, respectively. The results demonstrated significantly larger stress happening on the uncoated needle compared to the coated one. Also, the value of stress, that occurred in the needle, was two orders larger than that occurred in the soft tissue. Another interesting observation from their results is that the maximum stress in the tissue was detected at the cutting edge while the maximum stress in the needle was approximately spotted on its middle part. The deformation of the needle in lots of applications is negligible compared to the deformation of soft tissue since needles are usually much stiffer than soft tissues. However, sometimes needles are not that rigid and can deflect or remarkably deform during the insertion process.

ALE method is a suitable approach to investigate the deformational behaviour of needles while inserted into deep parts of soft materials. These models can be used in optimization studies and path planning algorithms. However, they use a solid–fluid interaction approach that is not completely a realistic model. Because tissue is in fact a deformable solid, while in ALE a flow of material is incorporated which is not what happens in real tissue deformation. Nevertheless, in addition to the capability of the ALE method for simulating large deformation of needle and tissue during the insertion procedure, another advantage of this method is that, in contrast to most models based on failure mechanisms, it can be efficiently modelled in a three-dimensional configuration. However, its effectiveness in modelling more complicated needles (e.g., jagged and harpoon-shaped needles) or more complex tissue models (e.g., multi-layer tissue or tissue with visco-hyperelstic constitutive models) has not yet been evaluated.

3.5 Coupled Eulerian–Lagrangian

Coupled Eulerian–Lagrangian (CEL) method is similar to ALE with the difference that in CEL the rezoned mesh is the original computational mesh whereas in ALE a new distinct mesh is generated [87]. Based on CEL formulation, initially, a Lagrangian step is executed in which element nodes are assumed to be temporarily true nodes of the deforming material. Then, an Eulerian step is executed in which the deformation is suspended while the elements are remeshed and the nodes always return to their original positions; meaning that the mesh does not move during the simulation. Using the CEL method, the element distortion during the cutting procedure is entirely resolved and there is no need to generate a conforming mesh [91]. Jushiddi et al. [92] simulated the insertion of a beveled tip biopsy needle (i.e., hollow cannula) into agar gel using a linear explicit dynamic CEL (Fig. 15a). Linear solid hexahedral elements and linear Eulerian brick elements were employed for discretizing needle and agar gel, respectively. Reduced integration and hourglass control were implemented for both types of elements. They investigated the needle deflection and the imposed contact stress on the needle from agar gel during the insertion process (Fig. 15b). Their results showed after puncture occurred in the agar gel, the maximum contact stress proceeded from the needle tip along the needle shaft. Also, they showed sharper needles led to lower peak forces (i.e., puncture forces) and larger needle deflections. The friction coefficient of 0.02 was found to best fit the experimental data, which is an order of magnitude lower than what was experimentally determined for the friction coefficient with agar gel. On the other hand, the insertion speed had little influence on the insertion force.

In another study, Jushiddi et al. [93] extended their CEL-based FE model to investigate the deflection and forces of a flexible hollow bevel tip needle. They simulated hollow needle insertion into a tissue-mimicking soft-gel and verified their simulations using experimental measurements of needle deflection and insertion forces. The hollow needle and agar gel were defined using Lagrangian and Eulerian elements, respectively. Therefore, the needle is considered a solid part while agar gel/tissue is defined as a viscous fluid (i.e., a fluidic portion or fluidic layer containing liquid with high viscosity). A penalty contact was also defined to model the interaction between them. In this approach, as long as the Eulerian volume fraction (EVF) is zero (void element), the needle can insert through the gel with no resistance until it encounters Eulerian elements filled with material ($EVF \neq 0$). Similar to their previous study [92], they studied needle deflection and contact distribution on needles from agar gel using different bevel angle needles. Their results showed lower bevel angle leads to larger deflection while the insertion force does not change significantly. On the other hand, although increasing the bevel angle from 15 ° to 60 ° changed the maximum contact stress along the needle surface, its effect did not follow a meaningful sequence with a predictable pattern.

Li et al. [94] also explored the effect of needle tip geometry on the needle deflection and tissue sampling length (or biopsy length which means the length that is needed to be able to successfully insert a needle to the suspicious area

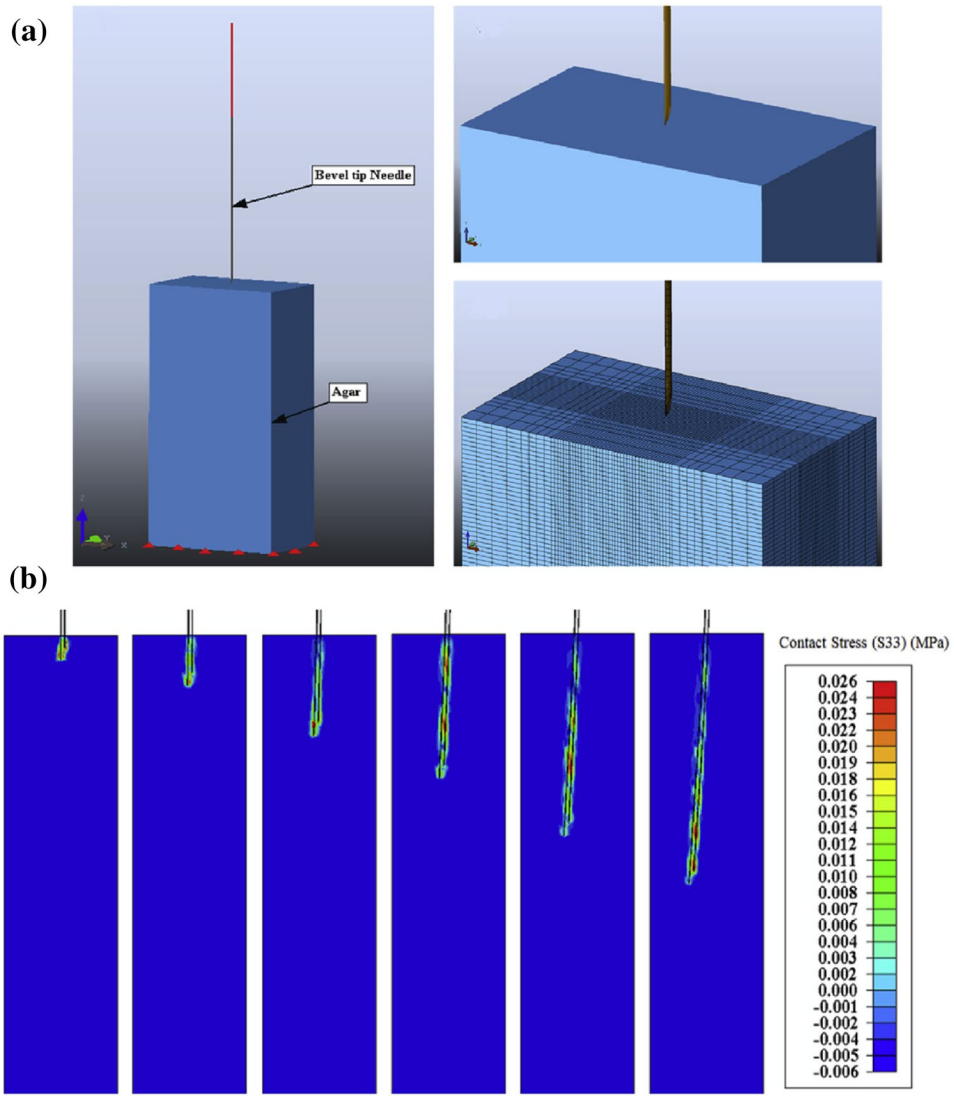

Fig. 15 FE modelling of needle insertion into a soft tissue phantom made of agar gel using CEL, Reprinted from [92] with permission from Elsevier: **a** geometrical configuration of the needle and gel and their meshing structure, **b** contact stress distribution for a bevel tipped needle with tip angle of 18° in different insertion depths

to extract a piece of tissue or sample of cells for laboratory examinations) using CEL-based FE analysis. They modelled the insertion of different tip types and experimentally verified their model with measurements of the needle deflection and biopsy sampling length performed in tissue-mimicking phantoms and ex vivo tissues. The needle motion was incorporated with a Lagrangian algorithm in their model, while the tissue was modelled with the Eulerian approach. As shown in Fig. 16a, they just included half of the needle and tissue in their FE model based on the geometrical symmetry of the insertion process. Eight-node linear cubical elements (EC3D8R) and ten-node quadratic tetrahedron elements (C3D10M) were used for meshing tissue and needle, respectively. The tissue-mimicking phantom (PVC) was considered to have linear elastic mechanical properties. The insertion process was modelled with a constant acceleration of 1333 m/s^2 and a friction coefficient of 0.18 was obtained for the contact between tissue and needle. The FE results obtained from their model for different types of needles (i.e., single-bevel, dual-bevel, vertical-bevel, and asymmetric multi-bevel needles) are shown in Fig. 16b. It was observed that the deformational behaviour of tissue and the distribution of stress around the needle tip and groove strongly depend on the geometrical shape of the needle. For example, a single-bevel tip separated the tissue to top and bottom surfaces, and generated a stress of 17 kPa on top of the needle and a 0 kPa stress on its bottom, whereas in dual-bevel tip the tissue at the bottom was also compressed leading to a more balanced

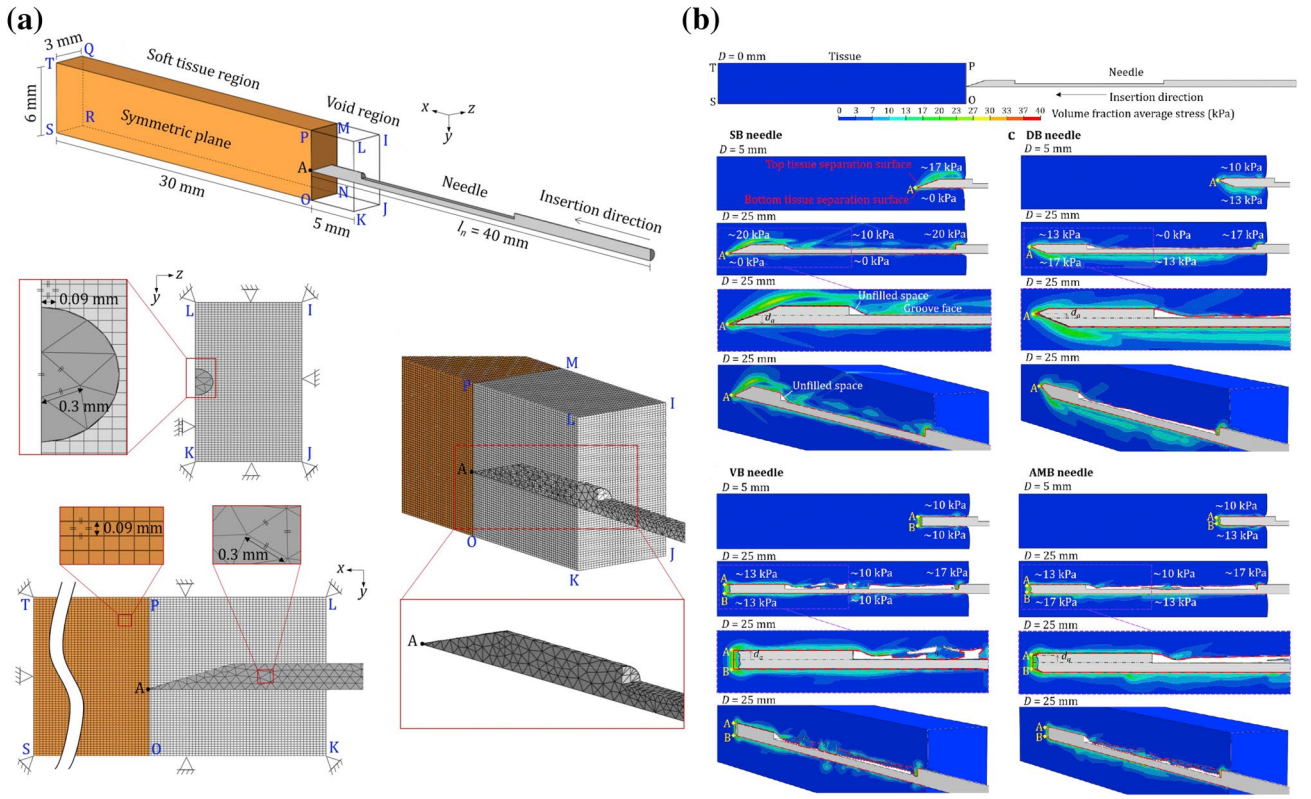

Fig. 16 FE modelling of a single-bevel tip needle insertion into a PVC phantom using CEL, Reprinted from [94] with permission from Elsevier: **a** model geometry and meshing structure, **b** the CEL results of needle insertion and tissue cutting for four different types of needles including single-bevel (SB), double-bevel (DB), vertical-bevel (VB), and asymmetric multi-bevel (AMB) needles

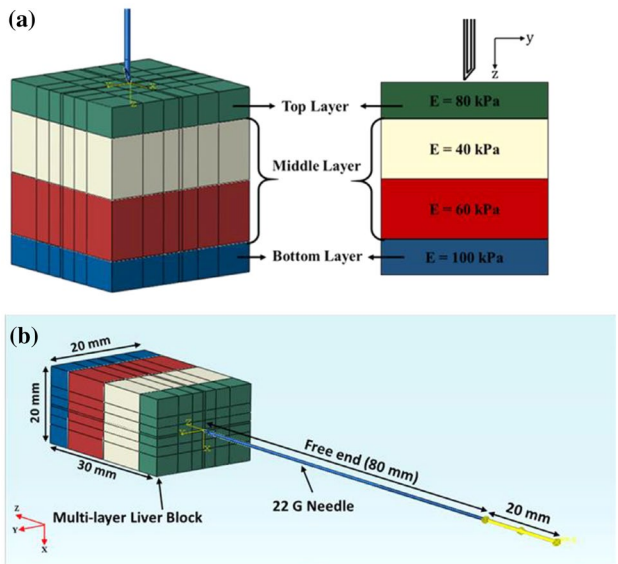

Fig. 17 FE modelling of needle insertion into a multilayer porcine liver using CEL, Reprinted from [95] with permission from Elsevier: **a** schematic of the multilayer model of the tissue, **b** solid model with a bevel needle fixed at rigid part and a free end in contact with the multilayer tissue block

stress distribution with values of 13, 0, and 17 kPa at the needle tip, front surface of the groove, and back surface of the groove, respectively.

More recently, another study by Jushiddi et al. [95] explored hollow needle insertion into a multilayer porcine liver tissue using CEL-based FE modelling. Their model contained a multilayer block representing the tissue which was fixed from all sides and a hollow needle which was positioned normal to the surface of the first layer. They performed experimental compression measurements and used empirically determined the Young's modulus for each layer of their model. Afterwards, they defined the thickness of all layers using the distribution of needle insertion data which was also acquired experimentally. The hollow needle was considered as a rigid part in their model and a displacement of 40 mm was applied to it to insert normally to the multilayer tissue block. All layers were meshed using eight-node solid linear Eulerian brick (EC3D8R) elements (Fig. 17). On the other hand, linear solid hexahedral (C3D8R) elements were used for meshing the needle. Reduced integration and hourglass control were implemented to all tissue and needle elements. They also incorporated friction between tissue and needle in

their model for which the coefficient of friction was set empirically.

Using the CEL method, usually one can take advantage of both Lagrangian and Eulerian methods. Therefore, it can be used as a very powerful tool in clinical applications like pre-operative surgical planning as it can provide results for the prediction of needle deflection, response forces, and the distribution of contact stress on the surface of the deformed needle in silico. It also has shown applicability in modelling needle insertion into multilayer tissues; this is very important especially when one of the layers is considerably more deformable than the others. Although the CEL approach eliminates the need for a conforming mesh and the element distortion issues in large deformations, the ambiguity of the boundary definition casts doubts on the reliability of interactions between the external boundaries and different parts (e.g., frictional contact between the needle and tissue). Another disadvantage of CEL modelling, which employs viscous fluid, is that it does not hold the puncture point force fixed during the tip insertion.

4 Real-Time Haptics

Although highly detailed models with advanced fracture method implementations usually provide accurate results, especially for complicated needle-tissue interaction models, simpler FE models have also been used for real-time medical applications. Real-time FE simulation of needle-tissue interaction can be used in haptic technologies, medical robotics, and virtual-reality training systems [96–98]. Here we briefly review some of the most recent related works in the literature.

Adagolodjo et al. [99] introduced an inverse FE simulation to control the needle insertion in deformable tissues in a real-time application. Their simulation combines a kinematic model of the robot, the FE models of the needle and deformable structure, and the interactions between them. They chose a phantom gel to represent the tissue and the robot was a 6-DOF Mitsubishi RV1A with 6 arms. The FE model was based on the co-rotational FE formulation in which the pure deformation of beam elements is separated from the rigid body motions and local deformations [100]. Linear tetrahedral elements were chosen for the discretization of the gel, whereas the needle was discretized with a set of linked beams. Both parts were modelled as a simple linear elastic material. The needle-tissue-robot interactions were implemented through three sets of constraints including bilateral, penetration, and sliding constraints.

Adebar et al. [101] investigated the effect of needle tip geometry (bent-tip length and angle) on the curvature of a steerable needle using a combination of FE modelling and experimental measurements with bent-tip needles in ex vivo porcine liver tissue. They employed a simplified two-dimensional FE model in which the needle was inserted and deformed the tissue, while the tissue rupture was eliminated from their model to make their FE model more tractable. They modelled the process with a static analysis step using the standard solver of ABAQUS. An incompressible Mooney–Rivlin hyperelastic material model was chosen for the tissue. Two types of elements including coarse quadrilateral elements (CPE4H), and finer triangular elements (CPE3H)—in the contact region—were used for the tissue. The needle's bent-tip was defined as a rigid body as it is usually made of steel or brass and is much stiffer than the tissue. In order to model the needle's shaft resistance to bending, a linear torsional spring was defined at the base of the rigid bent-tip. A horizontal movement was applied on the needle tip and its vertical displacement and rotation were measured after insertion. Their results showed an appropriate selection of bent-tip length and angle can advance the curvature of needles significantly. Also, based on the results of their FE simulations, they designed a new articulated-tip steerable needle, and performed validation tests on liver tissue that showed this new steerable needle can insert to the tissue with a smaller radius of curvature compared to the other needles introduced in previous studies.

Bui et al. [102] introduced the co-rotational cutting FE method for real-time surgical simulations using a background mesh of the tissue. The details of the simulated body surface, which were acquired from binary images, were exploited in a multilayer embedding algorithm to implement the cutting procedure. They used two types of boundary conditions in their simulation including Dirichlet and Neumann boundary conditions. The Lagrange multipliers and shape functions were employed in their model to define those boundary conditions. They verified their method by implementing various needle insertion simulations into the brain and liver models. They showed the proposed method is a suitable approach for patient-specific surgical simulations with suitable accuracy and low computational cost.

Adagolodjo et al. [103] implemented FE models in a close-control robotic loop applied to needle insertion procedure in order to take both tissue and needle deformations into account, and improve the accuracy of needle positioning. To this end, they numerically derived the Jacobian of the simulation using an inverse method and validated their

method numerically and experimentally using the insertion of a flexible needle into a deformable foam. The needle was simplified as a set of linked Timoshenko beams. Each beam segment was composed of two nodes and each node had 6 DOFs (position and rotation). Also, the geometry of the deformable foam was obtained from a segmentation procedure prior to the insertion and meshed with linear tetrahedral elements with four nodes each with 3 DOFs. They used a co-rotational formulation for the definition of the global stiffness matrix. The results of their study showed that using their proposed approach, the robot can follow a pre-determined trajectory while considering both needle and foam deformations during the insertion process.

Li et al. [104] proposed a methodology for needle steering in soft tissues based on a real-time FE model. Their method provides dynamic deformation information for online path planning of flexible needles. They formulated needle coordinates based on the transformations of a homogeneous matrix with quasi-static assumptions. They also performed real-time experiments of needle insertion into a polyvinyl alcohol (PVA) phantom tissue and recorded the trajectory using a Charge-Coupled Device (CCD) camera to validate their model. They developed an iterative approach to generate the feasible path by minimizing the general insertion error defined by an artificial potential field. Their results showed this method is helpful for real-time path planning of needle insertion into soft tissues.

5 Conclusions and Perspectives

The investigation of needle-tissue interactions using FE modelling can lead to more efficient and less irritating medical devices. Moreover, the cutting accuracy and efficiency of controlled needle insertion in robotic-assisted surgical systems and virtual-reality medical training systems can benefit from accurate needle-tissue interaction models. It is also highly beneficial to physicians to simplify medical and surgical procedures based on the feedback obtained from either real-time or non-real-time force–displacement responses of the FE models.

In this paper, we reviewed FE models of needle-tissue interactions including both models that consider damage mechanisms to emulate crack propagation in the tissue and models without any damage mechanisms with more focus on tissue deformation. We also presented a brief survey of the application of FE models in real-time haptics at the end of the paper. Table 1 summarizes all reviewed models' objectives, descriptions, and validation methods. Tissue and needle geometries and mechanical properties can be gleaned from Tables 2 and 3, respectively. Furthermore, all meshing strategies and solvers descriptions are encapsulated in Table 4.

The review of published models shows remarkable efforts for advancing FE methods to develop models of needle-tissue interaction. The models can be used for the development of novel diagnostic and therapeutic devices and for the evaluation of new technologies to facilitate medical procedures while reducing irritation and injuries in patients. However, the improvement of the previous models can unquestionably augment their efficacy:

- As most of the proposed models in the literature are validated based on phantom tissues rather than real biological tissues, their accuracy and applicability are still debatable. Establishing similar FE models based on needle insertion experiments into biological tissues can enhance the applicability of these models further.
- Non-invasive models can help to investigate the deformation characteristics of tissues and needles and to lay a solid foundation for invasive FE models. Although without implementing a damage mechanism, the non-invasive models of the tissue in different physiological and loading conditions have already been valuable and intricate enough to motivate many studies, applying more complicated algorithms based on invasive methods to these models with the same biological tissue will provide a better understanding of needle-tissue interactional behaviour. Although, these models have not been to the interest of researchers for modelling needle-tissue interactions, they have been used in some similar studies for damage and rupture modelling for soft tissues.
- Other than the reviewed methods in the current study, some other methods such as the extended finite element method (XFEM) [105–107] and the generalized finite element method (GFEM) [108] can be potentially used to deal with the generation of new crack surfaces when the needle inserts into the tissue. Although these methods have not been utilized for modelling needle-tissue interactions, they have been successfully used for other cutting and rupture studies. The applications of these methods for damage and rupture modelling for soft tissues, were recently reviewed [109, 110]. We also recently proposed a method based on the combination of experimental analyses with FE modelling by which the

Table 1 Objectives, validation methods, and modelling strategies (invasive or non-invasive) of different FE models reviewed in this paper

No	Reference	Main objectives	Needle-tissue model description	Validation method	Damage mechanism
1	Chanthasopeephan et al. [52]	Characterizing the deformation of the liver tissue using local effective modulus (LEM). Also, performing parametric study to investigate the effect of cutting speed and cutting angle on LEM	Both two-dimensional and three-dimensional Needle is not included in their model	Iterative solving of an inverse problem formulated with the experimental data and FE simulation was implemented to validate their model	Nodal separation
2	Aoyagi et al. [33]	Fabrication of biodegradable polymer needle with various tip angles, imitating the insertion mechanism of mosquito's proboscis using FE simulation, and investigation of stress concentration around the insertion point	Both two-dimensional and three-dimensional models Quarter model due to symmetrical conditions (in three-dimensional model) Needle embedded in the tissue	Experimental measurements were performed on fabricated PLA microneedles and its insertion behaviour into the silicone rubber was compared with real mosquito's proboscis insertion mechanism and FE simulated models	NA (embedded needle)
3	Misra et al. [1[7]	Investigating needle-tissue interaction forces for bevel-tip needles and the effect of needle tip bevel angle, linear and non-linear tissue elasticity, and tissue fracture toughness on the tip forces	Two-dimensional Needle tip modelled as a right triangle	Several needle insertion experimental measurements were performed on different phantom (soft and hard plastisol) and biological (porcine and chicken) tissues to see the change in insertion force versus needle displacement. It seems further independent experimental data is required for complete validation of their model	CZM (Bilinear TSL)
4	Wittek et al. [34]	Introducing a FE model that considers both geometric and material non-linearity as well as patient-specific modelling of preceding puncture of brain meninges that predicts the needle force accurately	Three-dimensional Brain model contains the main part enveloped by a layer of pia meter Needle is not included	Constitutive properties were determined from experimental measurements on tissue samples from the same bran. Force–displacement plots were used to compare FE results with the equivalent experiments	NA (without needle)
5	Kong et al. [55]	Prediction of the skin deformation and its failure and microneedle insertion force during the insertion using different thickness values and material properties for skin layers and various microneedle geometries (tip area, wall angle, and wall thickness)	Axisymmetric model Tapered microneedles Multilayer skin model including stratum corneum, dermis, and hypodermis layers	The needle force–displacement plot was compared to the experimental results reported by Davis et al. [56]	Element deletion: von Mises stress failure criterion
6	Chen et al. [60]	Investigating microneedle-skin interaction during the insertion to assess skin deformation and stress distribution around the cutting zone, as well as finding a suitable geometrical design for microneedles	Three-dimensional Multilayer skin model including stratum corneum, viable epidermis, dermis, and hypodermis layers	The force–displacement plot obtained by an FE model was verified with the equivalent results of needle insertion into mouse skin	Element deletion: ultimate strength

Table 1 (continued)

No	Reference	Main objectives	Needle-tissue model description	Validation method	Damage mechanism
7	Gokgol et al. [53]	Finding fracture toughness of soft tissues (bovine livers) based on the differences in the cutting tool geometry (needle diameter)	Two-dimensional Axisymmetric model incremental needle displacement	Needle insertion experiments performed on 3 bovine livers with 4 custom-made needles were validated with an FE model	Nodal separation (energy-based fracture mechanics approach by comparison of fracture work with viscoelastic work)
8	Oldfield et al. [74]	Developing a high-resolution FE model to simulate the insertion of a needle to soft tissue phantom using a cohesive approach and investigating the effect of coefficient of friction and cohesive parameters on the force–displacement plots and studying energy distribution in different phases of insertion	Two-dimensional (out-of-plane depth 15 mm) Plane strain Symmetric	Cohesive elements were calibrated to achieve an FE model that replicates the experimental data obtained by the insertion of a needle into gelatin phantom tissue	CZM (Bilinear TSL)
9	Oldfield et al. [77]	Investigation of the rate dependency of tool-tissue interaction through the examination of contact interactions, strain energy release rate, and deformation in the tissue	Two-dimensional (out-of-plane depth 156 mm) Plane strain Symmetric	FE model was calibrated with the experiments by comparison of force–displacement plots at different insertion rates	CZM (Bilinear TSL)
10	Tai et al. [78]	Investigation on the change in cutting force during the insertion of two needles with different geometries using a three-dimensional cohesive FE model	Three-dimensional 2 different needle geometries Two-part phantom tissue including a primary layer with cohesive elements and a support layer	Experimental measurements using both needle types were performed on PVC phantom tissue and force–displacement results were compared with FE results	CZM (Bilinear TSL)
11	Yamaguchi et al. [88]	Developing a model of needle insertion to investigate its deflection and insertion force, the shear stress distribution around the needle, and to estimate an optimal needle insertion path for preoperative surgical planning	Three dimensional Bevel needle	The needle deflection and insertion force were compared with experiments with a uniaxial manipulator	ALE
12	Assaad et al. [61]	Investigation of needle-tissue interactions in terms of forces and torques exerted on the needle as well as nodal displacement of the tissue under needle pressure	Three-dimensional Bevel-tipped needle	The tip-gel interaction forces and torques acquired from the simulations were compared with experimental data	Element deletion: Johnson–Cook damage model
13	Idkaidek and Jasiuk [39]	Acquiring a fast and accurate model of porcine liver deformation under interaction with a surgical tool using the study of the effects of implicit versus explicit analysis, element type, and mesh density on computation time	Three-dimensional Surgical knife Porcine liver (Geometry obtained by MRI scanning)	They compared the results obtained by explicit and implicit solvers using various types of elements and mesh density with each other	NA (Pre-puncture)

Table 1 (continued)

No	Reference	Main objectives	Needle-tissue model description	Validation method	Damage mechanism
14	Oldfield et al. [43]	Investigation of different motion profiles of the needle segments to determine methods that reduce target motion using insertion of a multi-segment needle into a pre-existing crack	Three-dimensional Conical tip needle	The simulation results were confirmed by experimental data acquired from the insertion needle to tissue phantom	NA (pre-existing crack)
15	Halabian et al. [45]	Studying the effect of insertion angle on the stress–strain field around the needle tip and sense of pain in patients	Three-dimensional Bevel-tip needle Geometry, configuration, and mechanical properties of the model adopted from Miller et al. 2013 [5] which was composed of slices of skin, soft tissues (i.e., fat, muscle, and ligament), and femoral artery	Injection on a group of 49 patients in different angles was performed experimentally and their sense of pain was considered as a criterion to compare with the strain and stress values in the corresponding FE model	NA (Pre-puncture)
16	Loizidou et al. [49]	Investigation of the structural characteristics and skin penetration of microneedles using arrays of microneedles with different geometries under force-controlled loading	Three-dimensional 3×3 microneedle arrays (triangular, square, or hexagonal base geometry for microneedles) Skin was considered as two cylindrical structures (stratum corneum & viable epidermis)	The deformed shape of microneedles in either FE model and experimental measurements were achieved and discussed	NA (Pre-puncture)
17	Peng et al. [63]	Analyzing biomechanical characteristics of needle insertion into cornea using a FE model based on distortion energy theory and investigation of the effect of needle speed on the insertion force	Two-dimensional Cornea is composed of two layers (epithelium and stroma) cornea is constrained by the sclera	The insertion of a needle into the cornea was performed experimentally and force–displacement plots were compared with the FE results	Element deletion: Distortion energy failure criteria (von Mises stress failure criterion)
18	Singh et al. [66]	Simulation of the insertion of coated neural probes into brain tissue to find buckling and insertion forces with sensitivity analysis of the geometrical and material properties	Three-dimensional probe and coating were coupled to each other	Parallel experiments on the insertion of a copper probe into tissue phantom and ex vivo brain tissues were performed and compared with modelling results	Element deletion: Shear strain threshold
19	Jiang et al. [69]	Investigating the effect of needle diameter, tip angle, and insertion speed on the penetration force into skin and stress and strain distribution in the tissue around the penetration point	Three-dimensional Human silica modelled as a cylindrical model around the insertion location	The insertion procedure was experimentally imitated using self-developed loading equipment	Element failure: failure strength
20	Konh et al. [89]	Prediction of the deflection and steering behaviour of a bevel-tip needle while inserting into soft tissue. Also, investigation on the effect of needle diameter and tip angle on its deflection in tissue	Solid–fluid interactions Three-dimensional Cylindrical needle Cuboid tissue with a void part surrounding the tissue	Three needle steering experiments in a soft phantom were carried out to validate the model by minimizing the error of predicted deflection compared to the value observed in the experiments	ALE (Skin puncture was not modelled)

Table 1 (continued)

No	Reference	Main objectives	Needle-tissue model description	Validation method	Damage mechanism
21	Amin et al. [47]	Evaluation of needle insertion using simulation with different needles with various injection angles and lengths to determine a suitable condition for insulin therapy in terms of patients' injury and pain	Three-dimensional Bevel-tip needle Two-skin layer which was connected through a remeshing process	No experimental measurement has been performed or chosen to validate the FE simulations	NA (Pre-puncture)
22	Jushiddi et al. [92]	Providing new insight into the biopsy needle and needle-tissue interactions. And studying the effect of bevel angle on the insertion force, contact stress, and needle deflection	-Three-dimensional Bevel tip needle Cube-shaped gel	The bevel-tip needle insertion into 3% agar gel with various tip angles was performed experimentally and the simulated needle deflection and insertion force were compared to the corresponding experimental results	CEL
23	Jushiddi et al. [93]	Modelling flexible hollow bevel tipped needle insertion into a biological mimetic gel. Also, Investigation of the effect of bevel tip angle on the insertion force, peak force, bending moment, contact stress, and needle deflection	Three-dimensional Bevel tip needle Cube-shaped gel	Needle deflection and insertion forces were compared with the corresponding experimental results	CEL
24	Gao et al. [90]	Investigation on the surface quality of the needle and its effect on insertion process (i.e., friction force, adhesion situation, and deformation of tissue) using PVP coating	Two-dimensional Bevel-tip needle	Extracorporeal insertion experiments were implemented to verify the accuracy of the FE model via a comparison of *axial* forces versus time in two different directions	ALE (Setting the fracture strain and displacement failure)
25	Li et al. [104]	Studying needle deflection and tissue sampling length in biopsy with different needle tip geometries and various tissue separation locations	Three-dimensional Symmetric model Different needle types	They investigated the needle deflection and tissue sampling length experimentally on *ex-vivo* tissues and tissue-mimicking phantoms to validate their model	CEL
26	Wang et al. [54]	Prediction of tissue deformation as well as deflection and bending angle of a flexible needle during the insertion process through a FE coupling model	Both two-dimensional and three-dimensional models Simplified needle modelled as a cantilever beam	Five markers were defined on the tissue in both modelling and experimental measurements and their displacements were compared to each other during the insertion process	Nodal separation (needle-tissue coupling process performed iteratively)

Table 1 (continued)

No	Reference	Main objectives	Needle-tissue model description	Validation method	Damage mechanism
27	Terzano et al. [80]	Simulation of the penetration of a steerable bevel-tip needle in brain-like gelatin with the prediction of penetration path using the distribution of strain energy density around the needle tip	Two-dimensional Plane strain Bevel-tip needle	They tuned TSL parameters so that the force–displacement curve matches the experiments presented by [74, 77] Their model was validated through the adjustment of offset-curvature trends of a programmable bevel-tip needle using the experiments performed by Burrows et al. [116]	CZM (bilinear TSL)
28	Radhika and Gnanavel [50]	Investigation on the characteristics (i.e., insertion depth, deformation of the microneedle, contact opening of the skin, and von Mises stress distribution) of different polymer-based microneedles during the insertion process into human skin	Three-dimensional Conical shaped microneedles	The experimental data of polycarbonate microneedle insertion into porcine skin available in [117] was used to validate the FE model based on the insertion depth against the force	NA (Pre-puncture)
29	Jushiddi et al. [95]	Implementing CEL-based FE modelling technique into a multilayer soft biological tissue (i.e., porcine liver) to investigate needle insertion into more complicated heterogeneous tissues compared to homogenous single layer tissues	Three-dimensional Hollow cannula needle	The needle insertion force and cutting force obtained from FE simulations were compared with experimental results of needle insertion into the porcine liver	CEL
30	Mohammadi et al. [83]	Modelling through-and-through needle insertion into human skin Developing an optimization algorithm to determine mechanical properties of the tissue and CZM parameters from parameter study on needle geometry and energy study on different components involved in the cutting procedure	Two-dimensional Plane strain Two-layer tissue including skin and subcutaneous layers	The experimental data of hypodermic needle insertion into human skin reported in [70] was exploited to validate a force–displacement plot using a three-stage optimization process	CZM (bilinear TSL)

Table 2 Tissue material properties of different FE models reviewed in this paper

No	Reference	Tissue material	Material model	Density	Young's modules	Poisson's ratio	Hyperelastic constants	Viscoelastic constants	Damage/failure parameters	Contact model	Coefficient of friction	Insertion velocity	Insertion depth
1	Chanthasopeephan et al. [52]	Pig liver	Linear elastic		Arbitrary magnitude	0.3[51] 0.5 [52]							
2	Aoyagi et al. [33]	Silicone rubber	Elastic		2.2 MPa	0.45				frictional	0.7		
3	Misra et al. [17]	Soft & hard plastisol gel, Porcine gel, Chicken breast tissue	Elastic & Neo-Hookean hyperelastic		10–35 kPa	0.45	C_{10} = 3.57–4.93 kPa		δ_c = 0.71 mm Fracture toughness: G_C = = 24.22–114.4 kN/m	frictionless		1.25 mm/s	0.35, 0.5 mm
4	Wittek et al. [34]	Swine brain	Brain tissue: Ogden-type hyperviscoelastic Properties from [35]				μ_0 = 210 Pa α = -4.7	g = 0.450 g_2 = 0.365 τ_1 = 0.5 s τ_2 = 50 s				1, 5 mm/s	10 mm
			Meninges (pia mater): Mooney-Rivlin hyperelastic				$C_1 = C_2$ = 13,000 Pa						
5	Kong et al. [55]	Human skin	SC: Incompressible, isotropic, hyperelastic (one term Neo-Hookean)	1300 kg/m^3 [118]			Stiffness: C_{10} = 7.2–26 MPa [57] & C_{10} = 10 MPa [56]		Failure stress: σ = 13–44 MPa [119] & σ = 37 MPa[56]:	Surface to surface Kinematic algorithm	0.42 [120]	1.1 mm/s	0.2 mm
			Dermis: Incompressible, isotropic, hyperelastic (one term Neo-Hookean)	1200 kg/m^3 [121]			C_{10} = 0.16 MPa [119]		Failure stress: σ = 7.3 MPa [58]	frictional	0.42 [120]		
			Hypodermis: Isotropic, elastic	971 kg/m^3 [58]	340 kpa [59]	0.48							
6	Chen et al. [60]	Mouse skin	Stratum corneum: 1st order Ogden hyperelastic	1300 kg/m^3	0.752 MPa [122]		α = 8.68 [122]			Eroding surfaces-to-surface contact model		0.6 mm/min	
			Viable dermis: 1st order Ogden hyperelastic	1200 kg/m^3	0.489 MPa [122]		α = 20.68 [122]						
			dermis: 1st order Ogden hyperelastic	1200 kg/m^3	7.33 MPa [122]		α = 57.89 [122]						
			Hypodermis: elastic	970 kg/m^3	0.034 MPa [122]								

Table 2 (continued)

No	Reference	Tissue material	Material model	Density	Young's modules	Poisson's ratio	Hyperelastic constants	Viscoelastic constants	Damage/failure parameters	Contact model	Coefficient of friction	Insertion velocity	Insertion depth
7	Gokgol et al. [53]	Bovine livers Silicone sample	Hyper-viscoelastic				$C_{10}=430.00 \pm 26.40$ $C_{01}=427.08 \pm 20.84$ $C_{20}=418.14 \pm 1.84$ $C_{11}=417.91 \pm 1.10$ $C_{02}=669.49 \pm 113.20$	$\alpha_1= 0.394 \pm 0.16$ $\alpha_2= 0.232 \pm 0.11$ $\tau_1= 2.12 \pm 2.09$ $\tau_2= 9.98 \pm 1.85$	Fracture toughness: $G_C=164 \pm 6$ J/m^2	COF FKN FTOLN	0.8	FEM: 0.5, 3 mm/step & Exp: 0.5, 3, 5 mm/s	20 mm
8	Oldfield et al. [74]	Gelatine tissue phantom	Linear elastic		7 kPa	0.475			$\delta_y= 7$ $\delta_0= 7.5$ mm Fracture toughness: $G_C=17.43$ J/m^2	Penalty contact algorithm Coulomb friction law	0.5	10 mm/s	160 mm
9	Oldfield et al. [77]	Gelatine tissue phantom	Viscoelastic Linear elasticity		10.4 kpa			Adopted from [35]	$\delta_y= 7$ $\delta_0= 7.5$ mm Fracture toughness: 1st insertion ($G_C=9.47$–25.57 J/m^2) Two-insertion cycles ($G_C=14.07$–37.10 J/m^2)	Penalty contact algorithm Coulomb friction law	0.33—0.47	0.25–2.0 mm/s	100 mm
10	Tai et al. [78]	soft polyvinyl chloride (PVC) phantom tissue	Linear elastic		30 kPa	0.4			$t_c=3$ kPa K = 0.6 GP/m Fracture toughness: $G_C=10$ J/m^2	frictionless	NA	0.2 mm/s	20 mm
11	Yamaguchi et al. [88]	3% Agar gel	Isotropic elastic–plastic		$\sigma-\varepsilon$ Plotted in their paper					frictional	0.01	2 mm/s	100 mm
12	Assaad et al. [61]	gel	Linear elastic		0.27 MPa	0.495			Yield stress: σ_y=49kpa Plastic strain: ϵ_p=0.004	frictional	0.68	1 mm/s	1 + 0.5 mm (depth + tip displacement)
13	Idkaidek and Jasiuk [39]	Porcine liver	Hyperelastic (third-order polynomial Ogden)			0.48	Adopted from Kemper et al. [42]						10 mm
14	Oldfield et al. [43]	Gelatine tissue phantom	Linear elastic		7 kPa	0.45				Penalty contact algorithm Coulomb friction law	0 – 0.3	0.5 mm/s	40 mm
15	Halabian et al. [45]	Human skin, soft tissues, and femoral artery	Elastic		Skin: 2.10 MPa Soft tissue: 0.11 MPa Vessel: 1.23 MPa	Skin: 0.30 Soft tissue: 0.30 Vessel: 0.25							

Table 2 (continued)

No	Reference	Tissue material	Material model	Density	Young's modules	Poisson's ratio	Hyperelastic constants	Viscoelastic constants	Damage/failure parameters	Contact model	Coefficient of friction	Insertion velocity	Insertion depth
16	Loizidou et al. [49]	ex vivo porcine skin	Linear elastic		Stratum corneum: 1 MPa [123] Viable epidermis: 1 MPa [123] Dermis: 0.066 MPa [124]	All parts: 0.495							$< 0.5\ \mu$ m (under 5N applied force)
17	Peng et al. [63]	Porcine Cornea	Stroma& epithelium: Visco-hyperelastic (Mooney-Rivlin/modified Maxwell: generalized Prony-series Sclera: Elastomer		Sclera: 3.08 MPa	0.49	Stroma & epithelium: $C_{10} = 10.59$ $C_{01} = 11.20$	Stroma& epithelium: (E1, E2, E3, E4, E5) = (0.69, 0.43, 0.31, 0.40, 0.43) MPa $(\tau_1, \tau_2, \tau_3, \tau_4) = (8.83, 65.33, 876.93, 2.84 \times 10^3)$ seconds	Stroma: 5 MPa Epithelium: 10 MPa	Surface-to-surface (explicit) Penalty contact algorithm Finite sliding Hard contact Modified Karnopp friction		1, 5 mm/s	0.7 mm
18	Singh et al. [66]	Tissue phantom of brain	Hyperelastic (Ogden)				Adapted from [67, 68]		Shear strain threshold: 0.05 (range: 0.01–0.25)	Surfaces-to-surface contact algorithm	0 – 0.5	0.1 mm/s	
19	Jiang et al. [69]	Medical silicone	Bilinear elasto-plastic	1100–1200 kg/m^3	2.2	0.45			Failure strength: 10 MPa Tear strength: 2.4–4.0 MPa	Face penetration with coulomb law	0.1 (or 0.7)		4 mm
20	Konh et al. [89]	-Soft phantom made of Plastisol gel -Close to prostate	Linear elastic	-	22.29 kPa 24.1 + 14.5 kPa	0.49				frictionless		Ramp function: 0–10 mm/s in 10 s	150 mm
21	Amin et al. [47]	Human skin	Linear elastic	-	2.1 MPa [45]	0.3 [45]					0.12 [125]		
22	Jushiddi et al. [92]	Agar gel	Elastic	1.172 g/cm^3	0.0279 MPa	0.49					0.02	2.5 & 4 mm/s	50 mm
23	Jushiddi et al. [93]	Agar gel	Elastic–plastic	1.172 g/cm^3	0.279 MPa	0.49			Yield stress: σ_y = 0.008 MPa Ultimate stress: σ_u = 0.25 MPa	General Penalty contact	0.25	2.5 mm/s	40 mm
24	Gao et al. [90]	Fresh porcine loin	Mooney-rivlin	1120 kg/m^3			$C_{10} = 4.75$ $C_{01} = -4.91$			Surface-to-surface using kinematic contact algorithm	Conventional needle: 0.42Coated needle: 0.03	8.4 mm/s	60.48 mm

Table 2 (continued)

No	Reference	Tissue material	Material model	Density	Young's modules	Poisson's ratio	Hyperelastic constants	Viscoelastic constants	Damage/failure parameters	Contact model	Coefficient of friction	Insertion velocity	Insertion depth
25	Li et al. [104]	PVC phantom tissue with ex-vivo porcine loin tissue	elastic	0.98 g/cm^3	21.3 kPa	0.45				frictional	0.18	Acceleration: 1333 m/s^2	25 mm
26	Wang et al. [54]	Polyvinyl Alcohol (PVA)	Elastic	-									70 mm
27	Terzano et al. [80]	Gelatin tissue phantom	Linear elastic		14.8 kPa	0.475			δ_{max}= 1 mm (tip diameter of needle) δ_c= 8 mm (needle diameter) Fracture toughness: G_C=1.1 J/m^2	Coulomb's frictional law Lagrange multiplier method	0.3		5 mm
28	Radhika and Gnanavel [50]	Porcine skin	Linear elastic		61.4 GPa	0.4				frictionless	0	1 m/s	<0.8 mm (F_{max}=40 N)
29	Jushiddi et al. [95]	Porcine liver	Linear elastic		Varied depending on the layer and strain rate	0.49				Frictionless & frictional (general penalty contact)	0.2	2.5 mm/s	40 mm
30	Mohammadi et al. [83]	Human skin	Skin: 1st order Ogden hyperelastic	1.02 g/cm^3					Cohesive parameter: $t_c = 2MPa$ $K = 5000MPa/mm$ $\delta_0 = 1.6mm$ Fracture toughness: G_C=1600 J/m^2	Hard contact and Coulomb's law of friction with penalty contact algorithm	0.05	1 mm/s	10 mm
			Subcutaneous tissue: Linear elastic	0.9 g/cm^3	0.5 MPa	0.49							

Table 3 Needle model details of different FE models reviewed in this paper

No	Ref	Material model	diameters	Tip angles	length	More details
1	Chanthasopeephan et al. [52]	NA				
2	Aoyagi et al. [33]	E = 190 GPa, ϑ=0.17	2D: width = 90, 120, 150, 230 μm 3D: Cross-section of 60 μm^2	2D: 10, 20, 30, 40 ° 3D: 30 °		
3	Misra et al. [17]	E = 50 & 200 kPa, ϑ =0.3	0.71, 2.0 mm	10–80 °		
4	Kong et al. [55]	Rigid body	60–1200 μm (tip diameter)			Tip length = 720 μm Wall angle = 50–90 ° Wall thickness = 3–30 μm Tip area = 5000–20000 μm^2
5	Wittek et al. [34]	Did not specified				
6	Chen et al. [60]	Rigid body	Base width = 100 μ m × 200 μ m	30 °	1000 μ m	
7	Gokgol et al. [53]		Exp: 2, 3, 4, 5 mm	Round tip & sharp tip Exp (12, 18, 24, 30 °)		
8	Oldfield et al. [74]	Rigid body	8 mm	50 °		
9	Oldfield et al. [77]	Rigid body	W = 4 mm	35 °		
10	Tai et al. [78]	Bias bevel tip	11-gauge	Bevel angle = 15 °		
		Lancet tip	11-gauge	1st bevel angle = 15 ° 2nd bevel angle = 5 ° Rotation angle = 60 °		
11	Yamaguchi et al. [88]	Copper needle C1100 (E = 117 GPa, ϑ = 0.33)		30, 45, 60 °		
12	Assaad et al. [61]	Steel (E = 200GPa)	1 mm	45 °	20 mm	
13	Idkaidek and Jasiuk [39]	Elastic properties of steel	Base width = 1 mm	Tapered at 0.54 ° with a rounded 0.1 mm radius tip		
14	Oldfield et al. [43]	Rigid	4 mm	20 °		
15	Halabian et al. [45]	Rigid				
16	Loizidou et al. [49]	Linear elastic: E = 3.5 GPa, ϑ = 0.3, ρ = 1.24 g/cm^3	Footprint diameter: 200 μm Tip diameter: 10 μm		Height: 800 μm	
17	Peng et al. [63]	Rigid body	Medical needle No. 2 (0.2 mm)			
18	Singh et al. [66]	SU-8: E = 2.4 GPa, ϑ = 0.32, ρ = 1190 kg/m^3 Parylene C: E = 5.6 MPa,, ϑ = 0.45, ρ = 1289 kg/m^3 Coating: E = 1.9 GPa,, ϑ = 0.42, ρ = 1290 kg/m^3	Dimension in a range of 2.5 μm – 320 μm	Range: 0–75 °	3500 μm	
19	Jiang et al. [69]	Rigid body	0.5, 0.7, 0.9, 1.2 mm	30 °, 50 °, 70 °, 90 °		
20	Konh et al. [89]		0.38, 0.51, 0.64 mm	20 °, 30 °, 40 °, 50 °, 60 °	150 mm	
21	Amin et al. [47]	E = 198.6 GPa, ϑ = 0.263 [126]	ID = 0.105 mm OD = 0.23 mm	3D shape available in the paper	4, 6 mm	
22	Jushiddi et al. [92]	Steel needle: E = 200 GPa, ϑ = 0.29	0.9 mm	18 °, 27 °	125 mm	Bevel length: 2.95 mm & 2.01 mm
23	Jushiddi et al. [93]	Stainless steel needle: E = 200 GPa, ϑ = 0.29	OD = 0.71 mm ID = 0.57 mm	15 °, 30 °, 45 °, 60 °, 90 ° (blunt)	300 mm	

Table 3 (continued)

No	Ref	Material model	diameters	Tip angles	length	More details
24	Gao et al. [90]	Flexible body: E = 194.02 GPa, ϑ = 0.3, ρ = 14,800 kg/m^3	1.6 mm	17 °	150 mm	
25	Li et al. [104]	AISI 316 stainless steel (Rigid)	1 mm (18-gauge)			Four different types of needles: refer to Fig. 2 and Fig. 3 of [94]
26	Wang et al. [54]	Not specified	0.8 mm (21 G)	20 °	200 mm	
27	Terzano et al. [80]	Linear elastic: E = 117–940 kPa ϑ = 0.475	8 mm	20 °		Tip radius: ρ_{tip} = 0.5 mm
28	Radhika and Gnanavel [50]	Linear elastic: Polycarbonate: E = 2.0 GPa, ϑ = 0.37 Polyurethane: E = 0.055 GPa, ϑ = 0.39 Silicon: E = 150 GPa, ϑ = 0.22	Tip diameter = 60 μ m Base diameter = 600 μ m		900 μ m	
29	Jushiddi et al. [95]	Stainless steel: E = 200 GPa, ϑ = 0.29	OD = 0.71 mm ID = 0.57 mm	15 °—30 °	100 mm	
30	Mohammadi et al. [83]	Rigid	0.19 – 1.17 mm	6 °—30 °		

cutting characteristics, fracture toughness, and deformational behaviour of thin viscoelastic membranes can be attained [111]. Moreover, besides the FE-based models, other methods such as crack phase-field, meshfree, and particle methods [110, 112] can be used for modelling needle-tissue interactions and tissue rupture, but they were not the target of the current review.

- With the progress of microneedles and expanding their medical applications, developing models of the insertion of microneedles into the tissue can be used to improve the design of microneedles to bolster their effectiveness. When it comes to FE analysis of microneedle-tissue interactions, non-invasive models and invasive models based on element failure have been specifically of the interest of researchers. However, the analysis of the deformation of microneedles which are usually made of softer materials compared to the traditional medical needles (e.g., polymeric microneedle instead of metallic needles), can be performed more effectively with other methods like ALE and CEL.
- In recent years, there was a tremendous increase in using arrays of microneedles on patches [113]. These patches can be used for different purposes such as drug delivery [114]. Therefore, the insertion of an array of microneedles into the tissue needs to be addressed through FE modelling to investigate the effects of parameters such as patch and microneedle dimensions, microneedle spacing, and the number of microneedles on the patch-tissue interaction. Unfortunately, no research has been found on the invasive models of the interaction of microneedle patches with soft tissues. This is probably due to the complexity of these models and their high computational costs.
- Most FE models of needle-tissue interactions for real-time haptic applications were two-dimensional models in simplified geometries. There also needs to be some studies on three-dimensional real-time FE models for haptic devices that account for more complicated topological considerations. Furthermore, advanced FE models considering inhomogeneous and non-linear properties, that are closer to the realistic mechanical properties of soft tissues, are yet required to achieve more accurate real-time haptic solutions.
- Adding to the complexity of geometry or mechanical properties in FE models can significantly increase the running time of simulations which makes them not suitable for real-time applications. Therefore, using machine learning algorithms based on models that can be trained using numerous FE modelling and be executed in a short period of time, can be alternatively employed to facilitate the use of FE models in real-time haptic applications [115]. By that means, time-consuming FE simulations need to be performed just once and their output results can be used as a reliable dataset for training deep neural networks. Depending on the application and parameters of interest, one might find each of the invasive or non-invasive models expedient to generate a distinguished dataset.

Table 4 Mesh information and solvers used in different FE models reviewed in this paper

No	Reference	Types of elements	No. of elements or size	Software	Solver	Further description
1	Chanthasopeephan et al. [52]	3D quadratic elements 2D quadratic elements 2D linear elements	3D: 480 2D: 120	ABAQUS	Quasi-static	Reduced integration
2	Aoyagi et al. [33]	Not mentioned		ANSYS		
3	Misra et al. [17]	Cohesive quadrilateral elements (COH2D4) Bulk quadrilateral elements (CPE4H) Bulk triangular elements (CPE3H)		ABAQUS		
4	Wittek et al. [34]	Hexahedral elements (eight-node bricks) Belytschko-Tsay shell elements [37]	Hexahedral elements:19,337 (minimum element size: 0.5 mm) Shell elements: 4401	LS-DYNA	Explicit dynamic	Reduced Gauss quadrature Stiffness based hourglass control
5	Kong et al. [55]	CAX4R; four-node elements		ABAQUS	Explicit: Quasi-static	
6	Chen et al. [60]	Solid 164 element:		ANSYS	Explicit dynamic	
7	Gokgol et al. [53]	2D axisymmetric elements (four-node rectangular & three-node triangular)		ANSYS		
8	Oldfield et al. [74]	2D four-node cohesive elements Linear four-node plane strain Linear three-node plane strain	Mesh size around the cohesive zone: 1.6 mm	ABAQUS	Explicit & Implicit: Quasi-static	
9	Oldfield et al. [77]	Linear triangular plane-strain elements Cohesive elements		ABAQUS	Explicit	
10	Tai et al. [78]	Tissue: eight-node hexahedral elements Zero-thickness cohesive elements Needle: shell elements		ABAQUS	Explicit	
11	Yamaguchi et al. [88]	Rectangular elements as shell (needle) Hexahedral elements as solid (tissue)	297,014 (size = 0.375 mm)	ANSYS LS-DYNA	Dynamic analysis	
12	Assaad et al. [61]	Eight-node brick elements	Mesh size: 0.05 – 0.5 mm	ABAQUS	Explicit	
13	Idkaidek and Jasiuk [39]	Hexahedral (first-order & second-order) Tetrahedral (first-order & second-order)	Different Meshing Strategies (116,371–899,153)	ABAQUS	Static implicit Quasi-static implicit Explicit dynamic	Increasing load rate Applying mass scale Reduced integration

Table 4 (continued)

No	Reference	Types of elements	No. of elements or size	Software	Solver	Further description
14	Oldfield et al. [43]	Eight-node hexahedral (around the crack) Four-node tetrahedral (Away from the crack)	Mesh size: 0.5 – 60 mm	ABAQUS	Quasi-static explicit	Reduced integration
15	Halabian et al. [45]	Eight-node linear brick (C3D8R) Ten-node quadratic tetrahedron (C3D10)	82,020–90933	ABAQUS	Static	
16	Loizidou et al. [49]			COMSOL Multiphysiscs	Structural Mechanics module	
17	Peng et al. [63]	Four-node bilinear axisymmetric quadrilateral elements (CAX4R)	16,923	ABAQUS	Explicit dynamic	VUMAT (for material failure criterion) Reduced-integration Distortion control Enhanced hourglass control
18	Singh et al. [66]	Eight-node elements (C3D8R)		ABAQUS	Explicit dynamic	Reduced-integration Adaptive meshing
19	Jiang et al. [69]	Hexahedral elements		ABAQUS		
20	Konh et al. [89]	Eight-node Solid elements (both tissue and needle) ALE elements (tissue)	Needle: 244 Tissue: 12,464 Void part: 4914	LS-DYNA		Scaled young's modulus Mass scaling
21	Amin et al. [47]	Not mentioned	Mesh size of: 0.12	Mimics 3-Matic Marc. Mentat		
22	Jushiddi et al. [92]	Needle: linear solid hexahedral elements Gel: linear Eulerian brick	340,000 (smallest size = 0.1 mm)	ABAQUS	Explicit dynamic	Reduced integration Hourglass control
23	Jushiddi et al. [93]	Needle: linear solid hexahedral (C3D8R) elements Gel: linear Eulerian brick (EC3D8R)	359,560 (smallest size = 0.1 mm)	ABAQUS	Explicit dynamic	Reduced integration Hourglass control
24	Gao et al. [90]			ABAQUS	Explicit dynamic	
25	Li et al. [104]	Tissue and void regions: eight-node linear cubical element (EC3D8R) Needles: ten-node quadratic tetrahedron elements (C3D10M)	Tissue element sizes: 0.09 mm Needle element sizes: 0.3 mm	ABAQUS	Explicit dynamic	
26	Wang et al. [54]	2D: quadrilateral elements 3D: hexahedral elements Needle: beam elements	Smallest size = 0.001 m	ABAQUS	Quasi-static	

Table 4 (continued)

No	Reference	Types of elements	No. of elements or size	Software	Solver	Further description
27	Terzano et al. [80]	Needle and gel: plane strain triangular elements (CPE3) Cohesive zone: Zero-thickness four-node cohesive elements (COD2D4)	Smallest element size around needle tip h: h/ρ_{tip}=0.5 (Then: h = 0.25 mm)	ABAQUS	Implicit static	-CTOD -MSED
28	Radhika and Gnanavel [50]	C3D10ten-node quadratic tetrahedron elements (4 integration points)		ABAQUS	Static	
29	Jushiddi et al. [95]	Tissue: eight-node, solid linear Eulerian brick (EC3D8R) Needle: linear solid hexahedral (C3D8R)	The smallest element size: 0.1 mm	ABAQUS		Reduced integration Hourglass control
30	Mohammadi et al. [83]	Needle: discrete rigid elements (R2D2) Skin: three-node linear plane strain triangle elements (CPE3) and four-node 2D cohesive elements (COH2D4) Subcutaneous tissue: four-node bilinear plane strain quadrilateral elements (CPE4R)	R2D2: 227 CPE3: 28,000 COH2D4: 34 CPE4R: 15,000 (minimum element edge size: 0.1 mm)	ABAQUS	Explicit dynamic	Reduced integration Distortion control Hourglass control

Acknowledgements This work was supported by the Natural Sciences and Engineering Research Council of Canada (RGPIN-2020-05522) and the Canada Foundation for Innovation (38964).

Declarations

Competing interests The authors have no competing interests to declare that are relevant to the content of this article.

References

1. Han P, Che D, Pallav K, Ehmann K (2012) Models of the cutting edge geometry of medical needles with applications to needle design. Int J Mech Sci 65:157–167. https://doi.org/10.1016/j.ijmecsci.2012.09.014
2. Sivamani RK, Liepmann D, Maibach HI (2007) Microneedles and transdermal applications. Expert Opin Drug Deliv 4:19–25. https://doi.org/10.1517/17425247.4.1.19
3. Faraji Rad Z, Prewett PD, Davies GJ (2021) An overview of microneedle applications, materials, and fabrication methods. Beilstein J Nanotechnol 12:1034–1046. https://doi.org/10.3762/bjnano.12.77
4. Krithiga R, Geetha P (2021) Breast cancer detection, segmentation and classification on histopathology images analysis: a systematic review. Arch Comput Methods Eng 28:2607–2619. https://doi.org/10.1007/s11831-020-09470-w
5. Peña E, Pérez del Palomar A, Calvo B et al (2007) Computational modelling of diarthrodial joints: physiological, pathological and pos-surgery simulations. Arch Comput Methods Eng 14:47–91. https://doi.org/10.1007/s11831-006-9001-3
6. Rodriguez JF, Alastrue V, Doblare M (2008) Finite element implementation of a stochastic three dimensional finite-strain damage model for fibrous soft tissue. Comput Methods Appl Mech Eng 197:946–958. https://doi.org/10.1016/j.cma.2007.09.017
7. Dixit P, Liu GR (2017) A review on recent development of finite element models for head injury simulations. Arch Comput Methods Eng 24:979–1031. https://doi.org/10.1007/s11831-016-9196-x
8. Jiang S, Li P, Yu Y et al (2014) Experimental study of needle–tissue interaction forces: effect of needle geometries, insertion methods and tissue characteristics. J Biomech 47:3344–3353. https://doi.org/10.1016/j.jbiomech.2014.08.007
9. Casanova F, Carney PR, Sarntinoranont M (2014) In vivo evaluation of needle force and friction stress during insertion at varying insertion speed into the brain. J Neurosci Methods 237:79–89. https://doi.org/10.1016/j.jneumeth.2014.08.012

10. Gittard SD, Chen B, Xu H et al (2013) The effects of geometry on skin penetration and failure of polymer microneedles. J Adhes Sci Technol 27:227–243. https://doi.org/10.1080/01694243.2012.705101
11. de Jong TL, Pluymen LH, van Gerwen DJ et al (2017) PVA matches human liver in needle-tissue interaction. J Mech Behav Biomed Mater 69:223–228. https://doi.org/10.1016/j.jmbbm.2017.01.014
12. Ankersen J, Birkbeck AE, Thomson RD, Vanezis P (1999) Puncture resistance and tensile strength of skin simulants. Proc Inst Mech Eng 213:493–501. https://doi.org/10.1243/0954411991535103
13. Kuropka P, Kobielarz M, Dudek A et al (2011) Determination of the mechanical properties of the skin of pig foetuses with respect to its structure. Acta Bioeng Biomech 13(2):37–43
14. Leibinger A, Forte AE, Tan Z et al (2016) Soft tissue phantoms for realistic needle insertion: a comparative study. Ann Biomed Eng 44:2442–2452. https://doi.org/10.1007/s10439-015-1523-0
15. Datla NV, Konh B, Koo JJY et al (2014) Polyacrylamide phantom for self-actuating needle–tissue interaction studies. Med Eng Phys 36:140–145. https://doi.org/10.1016/j.medengphy.2013.07.004
16. Abolhassani N, Patel R, Moallem M (2007) Needle insertion into soft tissue: a survey. Med Eng Phys 29:413–431. https://doi.org/10.1016/j.medengphy.2006.07.003
17. Misra S, Ramesh KT, Okamura AM (2008) Modeling of tool-tissue interactions for computer-based surgical simulation: a literature review. Presence Teleoperators Virtual Environ 17:463–491. https://doi.org/10.1162/pres.17.5.463
18. van Gerwen DJ, Dankelman J, van den Dobbelsteen JJ (2012) Needle–tissue interaction forces–a survey of experimental data. Med Eng Phys 34:665–680. https://doi.org/10.1016/j.medengphy.2012.04.007
19. Wang Y, Li W, Han P et al (2016) Contributions in medical needle technologies—geometry, mechanics, design, and manufacturing. Mach Sci Technol 20:1–43. https://doi.org/10.1080/10910344.2015.1133917
20. Indermun S, Luttge R, Choonara YE et al (2014) Current advances in the fabrication of microneedles for transdermal delivery. J Controlled Release 185:130–138. https://doi.org/10.1016/j.jconrel.2014.04.052
21. Sabri AH, Ogilvie J, Abdulhamid K et al (2019) Expanding the applications of microneedles in dermatology. Eur J Pharm Biopharm 140:121–140. https://doi.org/10.1016/j.ejpb.2019.05.001
22. Ma G, Wu C (2017) Microneedle, bio-microneedle and bio-inspired microneedle: a review. J Controlled Release 251:11–23. https://doi.org/10.1016/j.jconrel.2017.02.011
23. Takabi B, Tai BL (2017) A review of cutting mechanics and modeling techniques for biological materials. Med Eng Phys 45:1–14. https://doi.org/10.1016/j.medengphy.2017.04.004
24. Liu Z, Wang C, Chen Z, Sui J (2021) The advance of surgical blades in cutting soft biological tissue: a review. Int J Adv Manuf Technol. https://doi.org/10.1007/s00170-021-06615-4
25. Teoh S, Chui C (2008) Bone material properties and fracture analysis: needle insertion for spinal surgery. J Mech Behav Biomed Mater 1:115–139. https://doi.org/10.1016/j.jmbbm.2007.06.004
26. Troedhan A (2017) Cutting bone with drills, burs, lasers and piezotomes: a comprehensive systematic review and recommendations for the clinician. Int J Oral Craniofacial Sci. https://doi.org/10.17352/2455-4634.0000128
27. Marco M, Rodríguez-Millán M, Santiuste C et al (2015) A review on recent advances in numerical modelling of bone cutting. J Mech Behav Biomed Mater 44:179–201. https://doi.org/10.1016/j.jmbbm.2014.12.006
28. Gao D, Lei Y, Zheng H (2012) Needle steering for robot-assisted insertion into soft tissue: a survey. Chin J Mech Eng 25:629–638. https://doi.org/10.3901/CJME.2012.04.629
29. Ravali G, Manivannan M (2017) Haptic feedback in needle insertion modeling and simulation. IEEE Rev Biomed Eng 10:63–77. https://doi.org/10.1109/RBME.2017.2706966
30. Scali M, Pusch TP, Breedveld P, Dodou D (2017) Needle-like instruments for steering through solid organs: a review of the scientific and patent literature. Proc Inst Mech Eng [H] 231:250–265. https://doi.org/10.1177/0954411916672149
31. Li P, Yang Z, Jiang S (2018) Needle-tissue interactive mechanism and steering control in image-guided robot-assisted minimally invasive surgery: a review. Med Biol Eng Comput 56:931–949. https://doi.org/10.1007/s11517-018-1825-0
32. Corrêa CG, Nunes FLS, Ranzini E et al (2019) Haptic interaction for needle insertion training in medical applications: the state-of-the-art. Med Eng Phys 63:6–25. https://doi.org/10.1016/j.medengphy.2018.11.002
33. Aoyagi S, Izumi H, Fukuda M (2008) Biodegradable polymer needle with various tip angles and consideration on insertion mechanism of mosquito's proboscis. Sens Actuators Phys 143:20–28. https://doi.org/10.1016/j.sna.2007.06.007
34. Wittek A, Dutta-Roy T, Taylor Z et al (2008) Subject-specific non-linear biomechanical model of needle insertion into brain. Comput Methods Biomech Biomed Eng 11:135–146. https://doi.org/10.1080/10255840701688095
35. Miller K, Chinzei K (2002) Mechanical properties of brain tissue in tension. J Biomech 35:483–490. https://doi.org/10.1016/S0021-9290(01)00234-2
36. Miller K, Chinzei K (1997) Constitutive modelling of brain tissue: experiment and theory. J Biomech 30:1115–1121. https://doi.org/10.1016/S0021-9290(97)00092-4
37. Belytschko T, Lin JI, Chen-Shyh T (1984) Explicit algorithms for the nonlinear dynamics of shells. Comput Methods Appl Mech Eng 42:225–251. https://doi.org/10.1016/0045-7825(84)90026-4
38. Mooney M (1940) A theory of large elastic deformation. J Appl Phys 11:582–592. https://doi.org/10.1063/1.1712836
39. Idkaidek A, Jasiuk I (2015) Toward high-speed 3D nonlinear soft tissue deformation simulations using abaqus software. J Robot Surg 9:299–310. https://doi.org/10.1007/s11701-015-0531-2
40. Gao Z, Lister K, Desai JP (2010) Constitutive modeling of liver tissue: experiment and theory. Ann Biomed Eng 38:505–516. https://doi.org/10.1007/s10439-009-9812-0
41. Umale S, Deck C, Bourdet N et al (2013) Experimental mechanical characterization of abdominal organs: liver, kidney & spleen. J Mech Behav Biomed Mater 17:22–33. https://doi.org/10.1016/j.jmbbm.2012.07.010
42. Kemper AR, Santago AC, Stitzel JD et al (2010) Biomechanical response of human liver in tensile loading. Ann Adv Automot Med 54:15–26
43. Oldfield MJ, Leibinger A, Seah TET, Rodriguez y Baena F (2015) Method to reduce target motion through needle–tissue interactions. Ann Biomed Eng 43:2794–2803. https://doi.org/10.1007/s10439-015-1329-0
44. Finocchietti S, Nielsen M, Mørch CD et al (2011) Pressure-induced muscle pain and tissue biomechanics: a computational and experimental study. Eur J Pain 15:36–44. https://doi.org/10.1016/j.ejpain.2010.05.010
45. Halabian M, Beigzadeh B, Karimi A et al (2016) A combination of experimental and finite element analyses of needle–tissue interaction to compute the stresses and deformations during injection at different angles. J Clin Monit Comput 30:965–975. https://doi.org/10.1007/s10877-015-9801-9

46. Miller SF, Sanz-Guerrero J, Dodde RE et al (2013) A pulsatile blood vessel system for a femoral arterial access clinical simulation model. Med Eng Phys 35:1518–1524. https://doi.org/10.1016/j.medengphy.2013.04.010
47. Mohamed Amin S, Ramlee MH, Mohd Latip HF et al (2019) Finite element analysis of needle insertion angle in insulin therapy. Int J Automot Mech Eng 16:7512–7523. https://doi.org/10.15282/ijame.16.4.2019.21.0555
48. Ramlee MH, Sulong MA, Garcia-Nieto E et al (2018) Biomechanical features of six design of the delta external fixator for treating pilon fracture: a finite element study. Med Biol Eng Comput 56:1925–1938. https://doi.org/10.1007/s11517-018-1830-3
49. Loizidou EZ, Inoue NT, Ashton-Barnett J et al (2016) Evaluation of geometrical effects of microneedles on skin penetration by CT scan and finite element analysis. Eur J Pharm Biopharm 107:1–6. https://doi.org/10.1016/j.ejpb.2016.06.023
50. Radhika C, Gnanavel BK (2021) Finite element analysis of polymer microneedle for transdermal drug delivery. Mater Today Proc 39:1538–1542. https://doi.org/10.1016/j.matpr.2020.05.549
51. Chanthasopeephan T, Desai JP, Lau ACW (2003) Measuring forces in liver cutting: new equipment and experimental results. Ann Biomed Eng 31:1372–1382. https://doi.org/10.1114/1.1624601
52. Chanthasopeephan T, Desai JP, Lau ACW (2007) Modeling soft-tissue deformation prior to cutting for surgical simulation: finite element analysis and study of cutting parameters. IEEE Trans Biomed Eng 54:349–359. https://doi.org/10.1109/TBME.2006.886937
53. Gokgol C, Basdogan C, Canadinc D (2012) Estimation of fracture toughness of liver tissue: experiments and validation. Med Eng Phys 34:882–891. https://doi.org/10.1016/j.medengphy.2011.09.030
54. Wang L, Gao D, Fu J et al (2020) Simulation of coupling process of flexible needle insertion into soft tissue based on ABAQUS. Comput Mater Contin 64:1153–1169. https://doi.org/10.32604/cmc.2020.010073
55. Kong XQ, Zhou P, Wu CW (2011) Numerical simulation of microneedles' insertion into skin. Comput Methods Biomech Biomed Engin 14:827–835. https://doi.org/10.1080/10255842.2010.497144
56. Davis SP, Landis BJ, Adams ZH et al (2004) Insertion of microneedles into skin: measurement and prediction of insertion force and needle fracture force. J Biomech 37:1155–1163. https://doi.org/10.1016/j.jbiomech.2003.12.010
57. Wildnauer RH, Bothwell JW, Douglass AB (1971) Stratum corneum biomechanical properties I. influence of relative humidity on normal and extracted human stratum corneum. J Invest Dermatol 56:72–78. https://doi.org/10.1111/1523-1747.ep12292018
58. Duck FA (1990) Physical properties of tissue: a comprehensive reference book. Academic Press
59. Gerling GJ, Thomas GW (2005) The effect of fingertip microstructures on tactile edge perception. In: First joint eurohaptics conference and symposium on haptic interfaces for virtual environment and teleoperator systems. IEEE, Pisa, Italy, pp 63–72
60. Chen J, Li N, Chen S (2012) Finite element analysis of microneedle insertion into skin. Micro Nano Lett 7:1206–1209. https://doi.org/10.1049/mnl.2012.0585
61. Assaad W, Jahya A, Moreira P, Misra S (2015) Finite-element modeling of a bevel-tipped needle interacting with gel. J Mech Med Biol 15:1550079. https://doi.org/10.1142/S0219519415500797
62. Johnson GR, Cook WH (1985) Fracture characteristics of three metals subjected to various strains, strain rates, temperatures and pressures. Eng Fract Mech 21:31–48. https://doi.org/10.1016/0013-7944(85)90052-9
63. Peng S, Yang Y, Leiyu Z, Long H (2016) Biomechanical simulation of needle insertion into cornea based on distortion energy failure criterion. Acta Bioeng Biomech. https://doi.org/10.5277/ABB-00248-2014-02
64. Pandolfi A, Manganiello F (2006) A model for the human cornea: constitutive formulation and numerical analysis. Biomech Model Mechanobiol 5:237–246. https://doi.org/10.1007/s10237-005-0014-x
65. Su P, Yang Y, Xiao J, Song Y (2015) Corneal hyper-viscoelastic model: derivations, experiments, and simulations. Acta Bioeng Biomech 17(2):73–84
66. Singh S, Lo M-C, Damodaran V et al (2016) Modeling the insertion mechanics of flexible neural probes coated with sacrificial polymers for optimizing probe design. Sensors 16:330. https://doi.org/10.3390/s16030330
67. Normand V, Lootens DL, Amici E et al (2000) New insight into agarose gel mechanical properties. Biomacromol 1:730–738. https://doi.org/10.1021/bm005583j
68. El Sayed T, Mota A, Fraternali F, Ortiz M (2008) Biomechanics of traumatic brain injury. Comput Methods Appl Mech Eng 197:4692–4701. https://doi.org/10.1016/j.cma.2008.06.006
69. Jiang L, Huang Y, Pan C et al (2016) Research on Insertion Process of Medical Needle. In: Proceedings of the 2016 3rd international conference on materials engineering, manufacturing technology and control. Atlantis Press, Taiyuan
70. Shergold OA, Fleck NA (2005) Experimental investigation into the deep penetration of soft solids by sharp and blunt punches, with application to the piercing of skin. J Biomech Eng 127:838. https://doi.org/10.1115/1.1992528
71. de Borst R (2003) Numerical aspects of cohesive-zone models. Eng Fract Mech 70:1743–1757. https://doi.org/10.1016/S0013-7944(03)00122-X
72. Shakoor M, Trejo Navas VM, Pino Munõz D et al (2019) Computational methods for ductile fracture modeling at the microscale. Arch Comput Methods Eng 26:1153–1192. https://doi.org/10.1007/s11831-018-9276-1
73. de Oliveira LA, Donadon MV (2020) Delamination analysis using cohesive zone model: a discussion on traction-separation law and mixed-mode criteria. Eng Fract Mech 228:106922. https://doi.org/10.1016/j.engfracmech.2020.106922
74. Oldfield M, Dini D, Giordano G, Rodriguez y Baena F (2013) Detailed finite element modelling of deep needle insertions into a soft tissue phantom using a cohesive approach. Comput Methods Biomech Biomed Eng 16:530–543. https://doi.org/10.1080/10255842.2011.628448
75. Misra S, Reed KB, Douglas AS et al (2008) Needle-tissue interaction forces for bevel-tip steerable needles. In: 2008 2nd IEEE RAS & EMBS international conference on biomedical robotics and biomechatronics. IEEE, Scottsdale, AZ, USA, pp 224–231
76. Azar T, Hayward V (2008) Estimation of the fracture toughness of soft tissue from needle insertion. In: Bello F, Edwards PJE (eds) Biomedical Simulation. Springer, Berlin, pp 166–175
77. Oldfield MJ, Dini D, Jaiswal T, Rodriguez y Baena F (2013) The significance of rate dependency in blade insertions into a gelatin soft tissue phantom. Tribol Int 63:226–234. https://doi.org/10.1016/j.triboint.2012.08.021
78. Tai BL, Wang Y, Shih AJ (2013) Cutting force of hollow needle insertion in soft tissue. In: ASME 2013 International Manufacturing Science and Engineering Conference collocated with the 41st North American Manufacturing Research Conference. American Society of Mechanical Engineers Digital Collection
79. Feng J MICROGRINDING OF CERAMIC MATERIALS, 147
80. Terzano M, Dini D et al (2020) An adaptive finite element model for steerable needles. Biomech Model Mechanobiol 19:1809–1825. https://doi.org/10.1007/s10237-020-01310-x

81. Persson P-O, Strang G (2004) A simple mesh generator in MATLAB. SIAM Rev 46:329–345. https://doi.org/10.1137/S0036144503429121
82. Mohammadi H, Maftoon N (2021) A validated cohesive finite element analysis of needle insertion into human skin. Can Med Biol Eng Soc 44:4
83. Mohammadi H, Ebrahimian A, Maftoon N (2021) Fracture behaviour of human skin in deep needle insertion can be captured using validated cohesive zone finite-element method. Comput Biol Med 139:104982. https://doi.org/10.1016/j.compbiomed.2021.104982
84. Habraken AM, Cescotto S (1990) An automatic remeshing technique for finite element simulation of forming processes. Int J Numer Methods Eng 30:1503–1525. https://doi.org/10.1002/nme.1620300811
85. Movahhedy M, Gadala MS, Altintas Y (2000) Simulation of the orthogonal metal cutting process using an arbitrary Lagrangian-Eulerian finite-element method. J Mater Process Technol 9:1
86. Boscheri W (2017) High order direct arbitrary-Lagrangian–Eulerian (ALE) finite volume schemes for hyperbolic systems on unstructured meshes. Arch Comput Methods Eng 24:751–801. https://doi.org/10.1007/s11831-016-9188-x
87. Bakroon M, Daryaei R, Aubram D, Rackwitz F (2018) Multi-material arbitrary Lagrangian-Eulerian and coupled Eulerian-Lagrangian methods for large deformation geotechnical problems. In: Cardoso AS, Borges JL, Costa PA et al (eds) Numerical Methods in Geotechnical Engineering IX, 1st edn. CRC Press, pp 673–681
88. Yamaguchi S, Tsutsui K, Satake K et al (2014) Dynamic analysis of a needle insertion for soft materials: arbitrary Lagrangian–Eulerian-based three-dimensional finite element analysis. Comput Biol Med 53:42–47. https://doi.org/10.1016/j.compbiomed.2014.07.012
89. Konh B, Honarvar M, Darvish K, Hutapea P (2017) Simulation and experimental studies in needle–tissue interactions. J Clin Monit Comput 31:861–872. https://doi.org/10.1007/s10877-016-9909-6
90. Gao F, Song Q, Liu Z et al (2020) Influence of a biocompatible hydrophilic needle surface coating on a puncture biopsy process for biomedical applications. Coatings 10:178. https://doi.org/10.3390/coatings10020178
91. Ducobu F, Rivière-Lorphèvre E, Filippi E (2016) Application of the coupled Eulerian-Lagrangian (CEL) method to the modeling of orthogonal cutting. Eur J Mech - ASolids 59:58–66. https://doi.org/10.1016/j.euromechsol.2016.03.008
92. Jushiddi MG, Mulvihill JJE, Chovan D et al (2019) Simulation of biopsy bevel-tipped needle insertion into soft-gel. Comput Biol Med 111:103337. https://doi.org/10.1016/j.compbiomed.2019.103337
93. Jushiddi MG, Cahalane RM, Byrne M et al (2020) Bevel angle study of flexible hollow needle insertion into biological mimetic soft-gel: simulation and experimental validation. J Mech Behav Biomed Mater 111:103896. https://doi.org/10.1016/j.jmbbm.2020.103896
94. Li ADR, Plott J, Chen L et al (2020) Needle deflection and tissue sampling length in needle biopsy. J Mech Behav Biomed Mater 104:103632. https://doi.org/10.1016/j.jmbbm.2020.103632
95. Jushiddi MG, Mani A, Silien C et al (2021) A computational multilayer model to simulate hollow needle insertion into biological porcine liver tissue. Acta Biomater 136:389–401. https://doi.org/10.1016/j.actbio.2021.09.057
96. DiMaio SP, Salcudean SE (2003) Needle insertion modeling and simulation. IEEE Trans Robot Autom 19:864–875. https://doi.org/10.1109/TRA.2003.817044
97. DiMaio SP, Salcudean SE (2005) Interactive simulation of needle insertion models. IEEE Trans Biomed Eng 52:1167–1179. https://doi.org/10.1109/TBME.2005.847548
98. DiMaio SP, Salcudean SE (2005) Needle steering and motion planning in soft tissues. IEEE Trans Biomed Eng 52:965–974. https://doi.org/10.1109/TBME.2005.846734
99. Adagolodjo Y, Goffin L, de Mathelin M, Courtecuisse H (2016) Inverse real-time Finite Element simulation for robotic control of flexible needle insertion in deformable tissues. In: 2016 IEEE/RSJ international conference on intelligent robots and systems (IROS). IEEE, Daejeon, South Korea, pp 2717–2722
100. Macquart T, Scott S, Greaves P et al (2020) Corotational finite element formulation for static nonlinear analyses with enriched beam elements. AIAA J 58:2276–2292. https://doi.org/10.2514/1.J058441
101. Adebar TK, Greer JD, Laeseke PF et al (2016) Methods for improving the curvature of steerable needles in biological tissue. IEEE Trans Biomed Eng 63:1167–1177. https://doi.org/10.1109/TBME.2015.2484262
102. Bui HP, Tomar S, Bordas SPA (2019) Corotational cut finite element method for real-time surgical simulation: application to needle insertion simulation. Comput Methods Appl Mech Eng 345:183–211. https://doi.org/10.1016/j.cma.2018.10.023
103. Adagolodjo Y, Goffin L, De Mathelin M, Courtecuisse H (2019) Robotic insertion of flexible needle in deformable structures using inverse finite-element simulation. IEEE Trans Robot 35:697–708. https://doi.org/10.1109/TRO.2019.2897858
104. Li M, Gao D, Lei Y, Xu T (2020) Dynamic path planning for bevel-tip flexible needle insertion into soft tissue based on a real-time finite element model. Math Probl Eng 2020:1–13. https://doi.org/10.1155/2020/4512409
105. Belytschko T, Black T (1999) Elastic crack growth in finite elements with minimal remeshing. Int J Numer Methods Eng 45:601–620. https://doi.org/10.1002/(SICI)1097-0207(19990620)45:5%3c601::AID-NME598%3e3.0.CO;2-S
106. Moës N, Dolbow J, Belytschko T (1999) A finite element method for crack growth without remeshing. Int J Numer Methods Eng 46:131–150. https://doi.org/10.1002/(SICI)1097-0207(19990910)46:1%3c131::AID-NME726%3e3.0.CO;2-J
107. Mariano PM, Stazi FL (2005) Computational aspects of the mechanics of complex materials. Arch Comput Methods Eng 12:391–478. https://doi.org/10.1007/BF02736191
108. Strouboulis T, Babuška I, Copps K (2000) The design and analysis of the generalized finite element method. Comput Methods Appl Mech Eng 181:43–69. https://doi.org/10.1016/S0045-7825(99)00072-9
109. Gültekin O, Holzapfel GA (2018) A brief review on computational modeling of rupture in soft biological tissues. In: Oñate E, Peric D, de Souza NE, Chiumenti M (eds) Advances in Computational Plasticity: A Book in Honour of D. Roger J. Owen. Springer, Cham, pp 113–144
110. Chittajallu SNSH, Richhariya A, Tse KM, Chinthapenta V (2022) A review on damage and rupture modelling for soft tissues. Bioengineering 9:26. https://doi.org/10.3390/bioengineering9010026
111. Mohammadi H, Ebrahimian A, Maftoon N (2023) Cutting characteristics of viscoelastic membranes under hypodermic needle insertion. Int J Mech Sci. https://doi.org/10.1016/j.ijmecsci.2023.108717
112. Zhang LW, Ademiloye AS, Liew KM (2019) Meshfree and particle methods in biomechanics: prospects and challenges. Arch Comput Methods Eng 26:1547–1576. https://doi.org/10.1007/s11831-018-9283-2
113. Jamaledin R, Makvandi P, Yiu CKY et al (2020) Engineered microneedle patches for controlled release of active compounds:

recent advances in release profile tuning. Adv Ther 3:2000171. https://doi.org/10.1002/adtp.202000171
114. Jamaledin R, Yiu CKY, Zare EN et al (2020) Advances in antimicrobial microneedle patches for combating infections. Adv Mater 32:2002129. https://doi.org/10.1002/adma.202002129
115. Bishara D, Xie Y, Liu WK, Li S (2022) A state-of-the-art review on machine learning-based multiscale modeling. Arch Comput Methods Eng, Simulation, Homogenization and Design of Materials. https://doi.org/10.1007/s11831-022-09795-8
116. Burrows C, Secoli R, Rodriguez y Baena F (2013) Experimental characterisation of a biologically inspired 3D steering needle. In: 2013 13th international conference on control, automation and systems (ICCAS 2013). IEEE, Gwangju, Korea (South), pp 1252–1257
117. Lhernould MS, Deleers M, Delchambre A (2015) Hollow polymer microneedles array resistance and insertion tests. Int J Pharm 480:152–157. https://doi.org/10.1016/j.ijpharm.2015.01.019
118. Gardner TN, Briggs GAD (2001) Biomechanical measurements in microscopically thin stratum corneum using acoustics: biomechanical measurements in stratum corneum using SAM. Skin Res Technol 7:254–261. https://doi.org/10.1034/j.1600-0846.2001.70408.x
119. Hendriks FM, Brokken D, Oomens CWJ et al (2006) The relative contributions of different skin layers to the mechanical behavior of human skin in vivo using suction experiments. Med Eng Phys 28:259–266. https://doi.org/10.1016/j.medengphy.2005.07.001
120. Elkhyat A, Courderot-Masuyer C, Gharbi T, Humbert P (2004) Influence of the hydrophobic and hydrophilic characteristics of sliding and slider surfaces on friction coefficient: in vivo human skin friction comparison. Skin Res Technol 10:215–221. https://doi.org/10.1111/j.1600-0846.2004.00085.x
121. Mehta AK, Wong F (1973) Measurement of flammability and burn potential of fabrics. Fuels Research Laboratory, MIT, Cambridge
122. Crichton ML, Donose BC, Chen X et al (2011) The viscoelastic, hyperelastic and scale dependent behaviour of freshly excised individual skin layers. Biomaterials 32:4670–4681. https://doi.org/10.1016/j.biomaterials.2011.03.012
123. Geerligs M, van Breemen L, Peters G et al (2011) In vitro indentation to determine the mechanical properties of epidermis. J Biomech 44:1176–1181. https://doi.org/10.1016/j.jbiomech.2011.01.015
124. Hara Y, Masuda Y, Hirao T, Yoshikawa N (2013) The relationship between the young's modulus of the stratum corneum and age: a pilot study. Skin Res Technol 19:339–345. https://doi.org/10.1111/srt.12054
125. Cua AB, Wilhelm K-P, Maibach HI (2006) Frictional properties of human skin: relation to age, sex and anatomical region, stratum corneum hydration and transepidermal water loss. Br J Dermatol 123:473–479. https://doi.org/10.1111/j.1365-2133.1990.tb01452.x
126. Grujicic M, Zhao H (1998) Optimization of 316 stainless steel/alumina functionally graded material for reduction of damage induced by thermal residual stresses. Mater Sci Eng A 252:117–132. https://doi.org/10.1016/S0921-5093(98)00618-2